UNIVERSITY OF STUTTGART

BACHELOR THESIS

Design and Implementation of Magnetic Field Compensation Coils for Quantum Network Experiments

Author:
Vincent BEGUIN

Examiner:
Prof. Dr. Tilman PFAU

Supervisor:
Dr. Stephan WELTE

Quantum Network Node Group
5. Physikalisches Institut

Submitted to the University of Stuttgart in fulfillment of the requirements for the degree of
BACHELOR OF SCIENCE

April 1st, 2025

Declaration of Authorship

Hiermit versichere ich gemäß § 27 Abs. 7 der Prüfungsordnung der Universität Stuttgart für den Bachelorstudiengang Physik vom 31.07.2015,

- dass ich diese Arbeit mit dem Titel *„Design and Implementation of Magnetic Field Compensation Coils for Quantum Network Experiments"* selbstständig verfasst habe,
- dass ich keine anderen als die angegebenen Quellen verwendet und alle wörtlich oder sinngemäß aus anderen Werken übernommenen Aussagen als solche gekennzeichnet habe,
- dass die eingereichte Arbeit weder vollständig noch in wesentlichen Teilen Gegenstand eines anderen Prüfungsverfahrens gewesen ist und,
- dass das elektronische Exemplar mit den gedruckten Exemplaren übereinstimmt.

Stuttgart, April 1st, 2025 Vincent Beguin

Kurzfassung

Ein dreiachsiges Kompensationsspulensytem für die Verwendung in einem Quantennetzwerkexperiment wird entworfen und ein Teil des Systems in Form eines Prototypen realisiert. Die Designziele und Einschränkungen im Hinblick auf das angestrebte Experiment werden dargelegt. Es werden wichtige Eigenschaften wie die Magnetfeldstärke, die räumliche Ausdehnung des homogenen Magnetfeldvolumens, die Reaktionszeit des Systems und die Wärmeentwicklung im Betrieb berechnet und vermessen.

Der Prototyp wird überwiegend aus kommerziell erhältlichen Materialien gebaut und im Hinblick auf die genannten Eigenschaften charakterisiert.

Die Messungen des Magnetfelds wurden mit Hilfe eines dreiachsigen Magnetfeldsensors durchgeführt. Der Vergleich der Messungen mit den errechneten Werten ergibt für die Magnetfeldstärke als Funktion des angelegten Stroms mit $B/I = (4.032 \pm 0.009)\,\mathrm{G/A}$ eine gute Übereinstimmung mit der Theorie. Auch der Feldverlauf auf der zentralen Achse des Spulenpaars entspricht den Erwartungen. Für die Magnetfeldamplitude in der Fläche zwischen den Spulen wurde unerwartet ein Gradient in der vertikalen Richtung festgestellt. Diese Abweichung ist mutmaßlich auf die Tischoberfläche zurückzuführen auf der die Messung stattfand.

Die mit einem Präzisions-LCR-Meter durchgeführte Messung der Induktivität beider Spulen einzeln und des in Reihe geschalteten Paares decken sich mit den erwarteten Werten.

Die Reaktionszeit der Spulen auf sich ändernde Eingangsgrößen wurden zum einen durch die gemessenen Parameter, zum anderen anhand einer direkten Messung ermittelt und durch weitere direkte Messungen verifiziert. Die durch die direkte Messung ermittelte Reaktionszeit weicht über eine Größenordnung von der Vorhersage ab und weist daraufhin, dass die zur Beschreibung verwendete Theorie unvollständig ist.

Des Weiteren wurde die Wärmeentwicklung des Prototypen untersucht. Mittels der daraus extrahierten Werte für den Wärmetransferkoeffizienten in verschiedenen Laborbedingungen wurde die Vorhersage der vernachlässigbaren Temperaturentwicklung für den geplanten Betriebsbereich bestätigt.

Abstract

A triaxial compensation coil system for the use in a quantum network experiment is designed and part of the system is realized in the form of a prototype. The design goals and limitations with respect to the intended experiment are outlined. Important properties such as the magnetic field strength, the spatial extent of the homogeneous magnetic field volume, the response time of the system and the heat generation during operation are calculated and measured.

The prototype is mainly built from commercially available materials and characterized with regard to the properties mentioned.

The measurements of the magnetic field were carried out with a triaxial magnetic field sensor. The comparison of the measurements with the calculated values shows good agreement with the theory for the magnetic field strength as a function of the applied current with $B/I = (4.032 \pm 0.009)\,\mathrm{G/A}$. The field curve on the central axis of the coil pair also corresponds to expectations. For the magnetic field amplitude in the area between the coils, an unexpected gradient was found in the vertical direction. The deviation was presumably attributed to the table surface on which the measurement was carried out.

The measurement of the inductance of both coils individually and of the series-connected pair carried out with a precision LCR meter corresponds to the expected values.

The response time of the coils to changing input variables was determined on the one hand by the measured parameters and on the other hand by a direct measurement and verified by further direct measurements. The response time determined by the direct measurement deviates by an order of magnitude from the prediction and indicates that the theory used to describe it may be incomplete.

The heat development of the prototype was also investigated. The values extracted for the heat transfer coefficient in various laboratory conditions were used to confirm the prediction of negligible temperature development for the planned operating range.

Acknowledgments

I want to thank Prof. Dr. Pfau for sparking my interest in optics, atomic physics and quantum information and for giving me the opportunity to write my bachelor's thesis at the 5th Institut of Physics. I also want to thank Dr. Welte for giving the topic of the thesis, to work in his group and to experience how an experiment is designed from the ground up and contribute to that.

Many thanks to Raphael and Sebastián for supervising me during the thesis and for helping when questions arose.

I also want to thank the rest of the 5th Institut of Physics and the Welte group for letting me regularly borrow equipment and providing valuable tips around the making of coils.

Contents

1 Introduction

The construction of a quantum network promises technological advantage over networks which spread classical information [1, 2]. Besides the increase in security of data transmission through quantum key distribution [3], it also enables the possibility of distributed quantum computing [4]. These are important concepts for multi-party computation and for expanding the computational methods available, giving a way to solve problems classical computers are not capable of.

The advantage of quantum networks over classical networks results from the use of quantum mechanical properties such as entanglement and superposition for information processing [5–7]. This makes the practical implementation of even a single network node a difficult task, as the quantum properties are quite susceptible to decoherence [8]. Nowadays, several hardware platforms are being investigated. Besides attempts with trapped ions [9] or within solid-state systems like color centers in diamond [10], trapped neutral atoms within optical cavities offer promising platform for implementing such nodes [11].

The experiment of which this work is part of proposes to use trapped ^{87}Rb atoms coupled to an optical cavity to form a quantum network node, where the information is encoded in the hyperfine states of the atoms. The coupling to the optical cavity enhances the atom-light interaction and provides an interface to a photonic channel, through which several network nodes can be connected via fiber optic cables. The general feasibility of such a system with a single or two atoms has already been demonstrated in various studies [12–14], however, scaling up to a larger number of atoms remains a challenge. The focus of our experiment is on scaling this system to tens or hundreds of atoms coupled to the cavity by combining it with the well-studied optical tweezer platform [15]. With such a system, we aim to realize multi-qubit gates between atoms by reflecting a photon from the cavity [16], as well as to generate highly entangled photonic cluster states as a resource for various quantum network protocols [17].

To realize the described project, precise control over external magnetic fields is essential. Additionally, a constant guiding field along the cavity axis is needed for most experimental protocols. The guiding field provides a quantization axis for the atoms as well as a reference axis for the polarization of the photons, and can also be used to lift the degeneracy of Zeeman m_F states to enable the control of individual selected states via Raman transitions [11]. This work examines the possibilities to generate magnetic fields with good uniformity in a sufficiently big volume. The design of a triaxial system, consisting of three rectangular Helmholtz coil pairs to compensate for external magnetic fields, is laid out and a prototype coil pair is built. Measurements to characterize the prototype are conducted and the results are compared to calculations also done in this work.

This thesis is structured as follows. In Chapter 2, the theoretical foundation is laid to describe the atomic level structure and the generation of magnetic fields by current carrying coils. Also a model to describe the thermal characteristics of the coils is presented. Chapter 3 describes the design goals in more detail and the construction of the prototype, whose characterization measurement results are reported and discussed in Chapter 4. Chapter 5 summarizes the work and gives proposals for the future regarding, the experiment and the this work.

2 Theoretical Foundations

2.1 Atomic-Level Structure, Hyperfine and Zeeman Splitting

Atoms are not simple entities but rather complex systems governed by quantum mechanics, where electrons occupy discrete energy levels determined by their interaction with the nucleus. This complexity shows in the hyperfine interactions between the electrons and nuclear spins. The mathematically description of which is briefly described below follows [18].

The hyperfine structure is a result of the interaction between the total electron angular momentum[1] $\vec{J}$ and the total nuclear angular momentum $\vec{I}$[2]. This coupling leads to the total atomic angular momentum

$$\vec{F} = \vec{J} + \vec{I}, \tag{2.1}$$

where each energy level consist of $2F + 1$ degenerated magnetic sublevels, labeled by the quantum number m_F. The Hamiltonian which governs the hyperfine structure of the ^{87}Rb-D_2 line, shown in Figure 2.1, which will be used in the experiment, is

$$\mathcal{H}_{HFS} = A_{HFS}\vec{I} \cdot \vec{J} + B_{HFS}\frac{3(\vec{I} \cdot \vec{J})^2 + (3/2) \cdot \vec{I} \cdot \vec{J} - I(I+1)J(J+1)}{2I(2I-1)J(2J-1)}, \tag{2.2}$$

where A_{HFS} denotes the magnetic dipole constant and B_{HFS} the electric quadrupole constant. The resulting hyperfine energy shift is therefore

$$\Delta E_{HFS} = \frac{A_{HFS}K}{2} + B_{HFS}\frac{(3/2)K(K+1) - 2I(I+1)J(J+1)}{2I(2I-1)2J(2J-1)}, \tag{2.3}$$

with the abbreviation

$$K = F(F+1) - I(I+1) - J(J+1). \tag{2.4}$$

An external magnetic field $\vec{B}$ influencing the atoms is described by the Hamiltonian $\mathcal{H}_B$ and the g-factors as the electron spin g_S, electron orbit g_L and the nuclear spin g_I as

$$\begin{aligned} \mathcal{H}_B &= \frac{\mu_B}{\hbar}\left(g_S\vec{S} + g_L\vec{L} + g_I\vec{I}\right) \cdot \vec{B} && (2.5) \\ &= \frac{\mu_B}{\hbar}\left(g_S S_z + g_L L_z + g_I I_z\right) B_z, && (2.6) \end{aligned}$$

[1] Which itself originates from the coupling of the electrons orbital angular momentum $\vec{L}$ and its spin $\vec{S}$ as $\vec{J} = \vec{L} + \vec{S}$, resulting in the fine structure.

[2] It should be pointed out here that, in contrast to the rest of this work, the vector arrows here denote not simple vectors but vector operators.

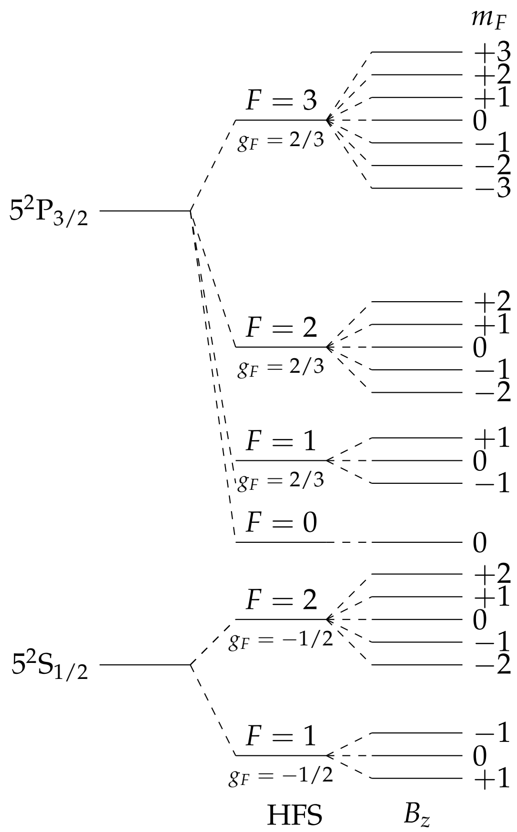

Figure 2.1: ^{87}Rb level structure of the hyperfine ground state $5^2S_{1/2}$ and excited state $^2P_{3/2}$. The lifting of the degeneracy due to a small magnetic field B_z is shown. The spacing of the sublevel depends on the g_F-factor and the magnetic quantum number m_F.

where for the second line $\vec{B} = B_z \cdot \hat{e}_z$ is assumed. Here μ_B is the Bohr magneton and $\hbar$ denotes the reduced Planck constant. For energy shifts induced by the magnetic field which are small compared to the hyperfine splitting, F can be approximated as good quantum number and the Hamiltonian can be written as

$$\mathcal{H}_B = \frac{\mu_B}{\hbar}\mu_B g_F F_z B_z, \tag{2.7}$$

with the Landé g-factor

$$g_F = \left(g_L \frac{\widetilde{J} - \widetilde{S} + \widetilde{L}}{2\widetilde{J}} + g_S \frac{\widetilde{J} + \widetilde{S} - \widetilde{L}}{2\widetilde{J}} \right) \frac{\widetilde{F} - \widetilde{I} + \widetilde{J}}{2\widetilde{F}} + g_I \frac{\widetilde{F} + \widetilde{I} - \widetilde{J}}{2\widetilde{F}}, \tag{2.8}$$

in which the abbreviation $\widetilde{\varkappa} = \varkappa(\varkappa + 1);\ \varkappa \in \{F, J, S, I\}$ is used.

For small static magnetic field magnitudes, this perturbation lifts the degeneracy of the sublevels according to their magnetic quantum number m_F

$$\Delta E_{|F,m_F\rangle} = \mu_B g_F m_F B_z\ , \tag{2.9}$$

which is known as the Zeeman effect.

For the hyperfine states used in the upcoming experiments, $|F=1\rangle$ and $|F=2\rangle$ in the $5^2S_{1/2}$ manifold, the Landé factors are $g_1 = -1/2$ and $g_2 = +1/2$, respectively. This results in a splitting of $\Delta E_{1,2}(m_F) = \mp 0.7\,\mathrm{MHz/G} \cdot m_F$. For the $5^2P_{3/2}$ manifold, all sublevels with $m_F \neq 0$ have $g_{1,2,3} = +2/3$, which results in $\Delta E_{1,2,3}(m_F) = 0.93\,\mathrm{MHz/G} \cdot m_F$ [18] .

2.2 Earth's Magnetic Field

To understand the need of a triaxial magnetic compensation system the origin of the disturbing field is explained and the magnitude is estimated.

The origin of the earth's magnetic field has long been an unsolved problem; even Einstein described it in his *annus mirabilis* as one of the great unsolved problems of physics at that time [19]. The case remained unresolved until 1958 when the three dimensional dynamo action was proofed by Herzenberg [20]. This makes the geodynamo theory, first proposed by Larmor and Josephs in 1919 [21], the best explanation for the observed presence of earth's magnetic field. Geodynamo theory describes the rotation of the liquid outer core of the earth around the solid inner core. Due to an interplay of physical forces and temperature differences, the liquid inner core consisting of conductive molten metal, forms helicoidal patterns which act like big solenoids which form the magnetic field.

A useful approach to describe earth's magnetic field is to split the whole vector field up in its main components. The field can be decomposed into a vertical component B_r and a horizontal component B_θ , which themselves are composed of the cartesian components as shown in Figure 2.2a. With basic euclidean geometry the following relations can be found:

$$|\vec{B}| = B = \sqrt{B_\theta^2 + B_z^2} = \sqrt{B_x^2 + B_y^2 + B_z^2}, \tag{2.10}$$

$$B_\theta = B\cos(J), \tag{2.11}$$

$$B_x = B_\theta \cos(D), \tag{2.12}$$

$$B_y = B_\theta \sin(D), \tag{2.13}$$

$$B_z = B_r = B_\theta \tan(J), \tag{2.14}$$

$$\tag{2.15}$$

where B denotes the magnitude, the angle J the inclination and D the declination [22]. Approximating the geodynamo as a homogeneously magnetized sphere with magnetic dipole moment $\vec{M} = m\vec{\delta}$, and neglecting higher order terms, the magnetic potential can be written as [22]

$$V = \frac{\mu_0}{4\pi}\frac{\vec{M}\cdot\vec{r}}{r^3}\,. \tag{2.16}$$

Using potential theory the magnetic field components in polar coordinates result in

$$\begin{aligned} B_z = B_r &= -\frac{\partial V}{\partial r} = \frac{\mu_0}{2\pi}\frac{M\cos(\theta)}{r^3}\,, \\ B_h = B_\theta &= -\frac{1}{r}\frac{\partial V}{\partial \theta} = \frac{\mu_0}{4\pi}\frac{M\sin(\theta)}{r^3}\,, \end{aligned} \tag{2.17}$$

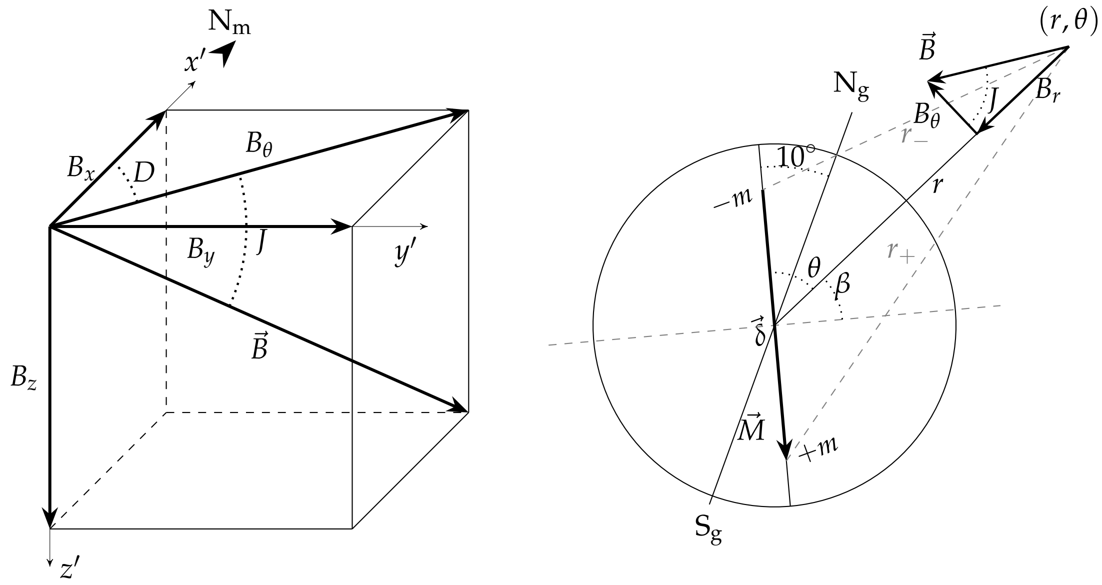

(a) **(b)**

Figure 2.2: **(a)** Composition of earth's magnetic field $\vec{B}$ from its polar components B_θ and B_z and also the cartesian components B_x, B_y and B_z. The orientation is chosen along the magnetic north pole $\mathrm{N_m}$ by convention. The inclination J and declination D angles are marked. **(b)** Earth modeled as dipole sphere with the magnetic dipole moment $\vec{M}$ as a result of the dipole strength $\pm m$ at a distance $\vec{\delta}$. The geographic north pole is shown as $\mathrm{N_g}$ the geographic south pole as $\mathrm{S_g}$. The tilt of the magnetic axis against the geographical axis of about 10° is shown. This defines the magnetic latitude β and magnetic pole height θ which are connected as $\beta = (\pi/4) - \theta$. An example magnetic field vector $\vec{B}$ and its components are shown. Figures taken from [22].

and therefore the magnitude is given by

$$B = \frac{\mu_0}{4\pi}\frac{M}{r^3}\sqrt{1 + 3\cos^2(\theta)}\ . \tag{2.18}$$

The course of the described magnetic field components is shown in Figure 2.3.

Because the magnetic and geographic coordinate systems are tilted against each other, illustrated in Figure 2.2b, a connection between the magnetic latitude β and the geographical latitude ϕ and respectively the geographical longitude λ is given by

$$\sin(\beta) = \sin(\phi_B)\sin(\phi) + \cos(\phi_B)\cos(\phi)\cos(\lambda - \lambda_B), \tag{2.19}$$

where ϕ_B and λ_B are the boreal geomagnetic poles [23]. Since the laboratory where the experiment takes place is located at ϕ =48.7452°N, λ =9.1034°E, the expected magnitudes B^{Ins} are

$$\begin{aligned} B^{\mathrm{Ins}} &= 0.488\,\mathrm{G}, \\ B_z^{\mathrm{Ins}} &= -0.448\,\mathrm{G}, \\ B_h^{\mathrm{Ins}} &= 0.193\,\mathrm{G}. \end{aligned} \tag{2.20}$$

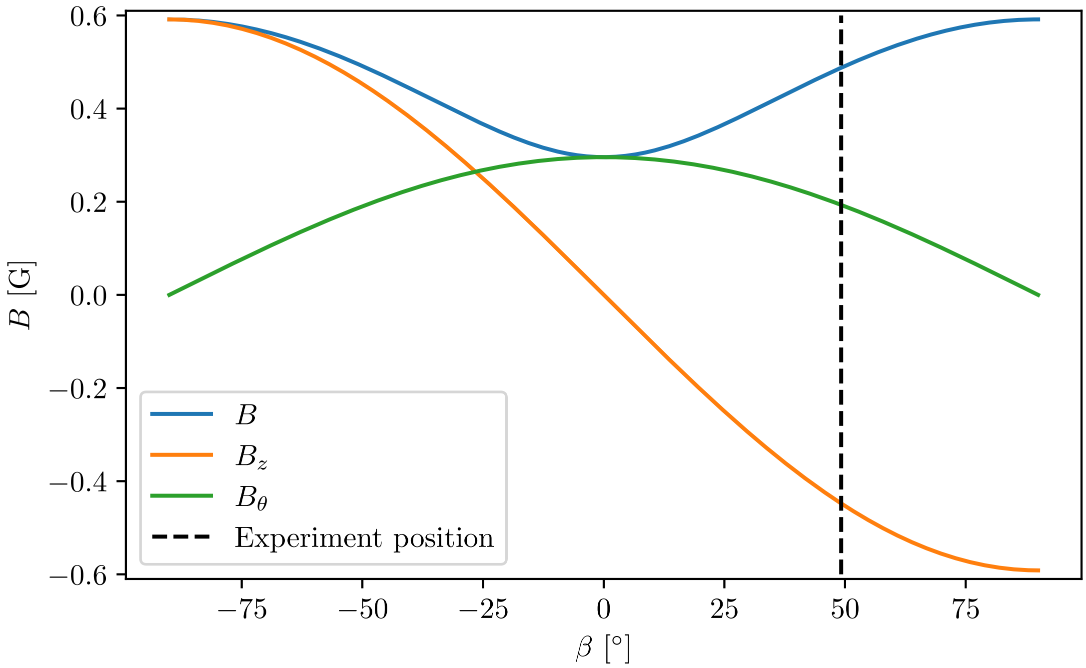

Figure 2.3: Magnitude of earth's magnetic field components B_z and B_θ , derived from Equation 2.17, as well as the resulting absolute value B, see Equation 2.18, in dependence of their position in the magnetic reference frame as defined in Figure 2.2b. The location where the experiment takes place is marked by the dashed line.

These values are not static, but show trends on different time scales. A short term behaviour where the magnetic field varies by 0.5 m G with an period of around 24 with the minimum amplitude at around mid day [24]. And a long term trend increasing by 0.24 m G per year, measured over the course of the last ten years [24]. Additional to the mentioned variations are also less predictable fluctuations, mainly due to solar activity. These can vary a lot in magnitude and time scale so that no general statement about the behavior can be made but live data is readily available [25].

This dipole sphere model approach represents only a first order approximation of the rather complex shape of earth's magnetic field, although sufficient for the estimations needed in this work [3].

This description of earth's magnetic field shows that each component must be manipulated individually and which magnitude is expected of each component.

2.3 Classical Electrodynamics

In the following, a formalism for the calculation of magnetic fields, generated by arbitrary current arrangements, is derived from the basics of classical electrodynamics.

[3] A more precise description can be achieved by using Laplace's equation on the magnetic potential term and developing this expression into spherical functions. By extracting the coefficients of the spherical functions from real world magnetic field measurements a rather precise description of earth's magnetic field is obtained, which is indeed done by the science branch of magnetic earth observation [23].

The fundamental description of classical electromagnetic phenomena is given by Maxwell's Equations [26]

$$\nabla \times \vec{E} = -\frac{\partial \vec{B}}{\partial t}, \tag{2.21}$$

$$\nabla \times \vec{B} = \mu_0 \vec{j} + \frac{1}{c^2}\frac{\partial \vec{E}}{\partial t}, \tag{2.22}$$

$$\nabla \cdot \vec{E} = \frac{\rho}{\varepsilon_0}, \tag{2.23}$$

$$\nabla \cdot \vec{B} = 0, \tag{2.24}$$

which describes the spatial distribution and time evolution of the magnetic field $\vec{B}$ and the electric field $\vec{E}$ with the constants of electrical vacuum permittivity ε_0 , magnetic vacuum permittivity μ_0 and the vacuum speed of light c for a given charge density ρ and current density $\vec{j}$.

This description can be simplified by introducing the vector potential $\vec{A}$ of the magnetic field as [27]

$$\vec{B} = \nabla \times \vec{A}, \tag{2.25}$$

with the nabla operator ∇, whose components are the first partial derivatives. This definition satisfies Equation 2.24 by construction. To fully determine the vector potential an additional condition is needed. By choosing the so called Coulomb Gauge

$$\nabla \cdot \vec{A} = 0, \tag{2.26}$$

and the relation

$$\nabla \times (\nabla \times \vec{A}) = \nabla(\nabla \cdot \vec{A}) - \nabla \cdot (\nabla \vec{A}) = -\Delta \vec{A}\,, \tag{2.27}$$

the Poisson equation

$$\Delta \vec{A} = -\mu_0 \cdot \vec{j}, \tag{2.28}$$

is obtained, which is solved by

$$\vec{A}(\vec{r}) = \frac{\mu_0}{4\pi} \int \frac{\vec{j}(\vec{r}')}{|\vec{r} - \vec{r}'|} \mathrm{d}V'. \tag{2.29}$$

Here the integration takes place over the whole current-carrying Volume V'.

Using Equation 2.25 the expression

$$\vec{B}(\vec{r}) = \frac{\mu_0}{4\pi} \int \nabla \times \frac{\vec{j}(\vec{r}')}{|\vec{r} - \vec{r}'|}\, \mathrm{d}V' \tag{2.30}$$

$$= \frac{\mu_0}{4\pi} \int \left(\vec{j}(\vec{r}') \times \frac{(\vec{r} - \vec{r}')}{|\vec{r} - \vec{r}'|^2} \right) \frac{1}{|\vec{r} - \vec{r}'|^2}\, \mathrm{d}V', \tag{2.31}$$

for the calculation of the magnetic field is obtained. Equation 2.31 is a very powerful equation, as it can theoretically be used to calculate the magnetic field of arbitrary current distributions. In practice, only a few highly symmetrical geometries can be calculated analytically. For more complex geometries, numerical methods such as finite element method must be used. By using numerical methods the precision depends only on the computational power.

For some cases simplifications can be made which reduces the computational effort. If the current density is located only in a thin volume, i.e. the current I flows through a thin wire with cross sectional area $\vec{S}$ and infinitesimal length element $\mathrm{d}\vec{l}$, the integration can be written as

$$\vec{j} \cdot \mathrm{d}V = \vec{j} \cdot \mathrm{d}\vec{S} \cdot \mathrm{d}\vec{l} \tag{2.32}$$

$$= I \cdot \mathrm{d}\vec{l}. \tag{2.33}$$

Then the integral in Equation 2.31 can be written as a line integral:

$$\vec{B}(\vec{r}) = \frac{\mu_0 \cdot I}{4\pi} \int \frac{1}{|\vec{r} - \vec{r}'|^2} \left(\frac{(\vec{r} - \vec{r}')}{|\vec{r} - \vec{r}'|^2} \times \mathrm{d}\vec{l} \right). \tag{2.34}$$

This is known as the Biot-Savart Law and is used in this work to describe and calculate the magnetic field of coils, which are essentially composed of thin current-carrying wires.

Magnetic Field of a Straight Wire

Using the Biot-Savart law for a straight wire with length $2a$, positioned symmetrically on the x'-axis as shown in Figure 2.4, the resulting magnetic field is

$$\vec{B}_{\text{wire}} = \frac{\mu_0 I}{4\pi \cdot s} \left(\sin(\theta_2) - \sin(\theta_1) \right) \hat{\vec{s}} \times \hat{\vec{x}}, \tag{2.35}$$

with the vectors of unit length $\hat{\vec{s}}$ and $\hat{\vec{x}}$ and the angles θ_1, θ_2 defined as

$$\sin(\theta_1) = \frac{(x-a)}{\sqrt{(x-a)^2 + s^2}}, \tag{2.36}$$

$$\sin(\theta_2) = \frac{(x+a)}{\sqrt{(x+a)^2 + s^2}}, \tag{2.37}$$

$$\hat{\vec{s}} \times \hat{\vec{x}} = \left(0,\ z/\sqrt{y^2+z^2},\ -y/\sqrt{y^2+z^2} \right)^T. \tag{2.38}$$

Noteworthy here is the absence of a magnetic field component in x direction. These straight line description lays the foundation for constructing more complex shapes. Due to the linearity of Maxwell's equations, the superposition principle can be used to obtain the generated magnetic field of an entire arrangement by the sum of its individual parts:

$$\vec{B} = \begin{cases} \sum_i^n \vec{B}_i & \text{in general} \\ n \cdot \vec{B} & \text{if } \vec{B}_i = \vec{B}_{i+1}\ \forall\ i \end{cases} \tag{2.39}$$

where the second case holds if the geometric shape and the carried current of all of the n wire pieces are identical.

As shown, the shape of every magnetic field, which satisfies Equation 2.24, can be produced by using geometric arrangements of current-carrying wires.

To obtain certain properties of the magnetic field like uniformity and specified magnitude some conditions must be met by geometric parameters and the current applied to the wires.

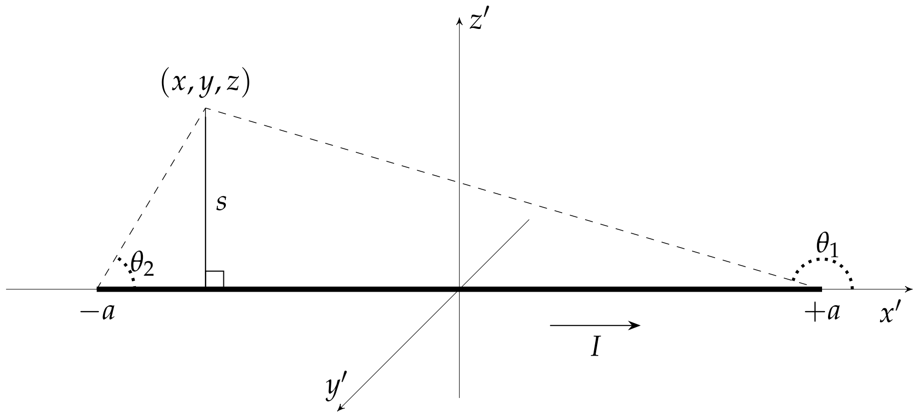

Figure 2.4: Thin wire of side length $2a$ placed symmetrically at the x-axis flowed through by current I. Auxiliary quantities such as the angles θ_1, θ_2 and the distance s from a point at (x, y, z) are also shown to simplify the description of the arrangement by the Biot-Savart law.

2.4 Helmholtz Coil Arrangement

In this section the theory behind the creation of uniform magnetic fields with rectangular coils in a Helmholtz arrangement will be explained. Explicit expressions are deduced from the general description given by Equation 2.34 and particular useful relationships are derived.

Multiple different arrangements like Merrit [28], Maxwell [29] or Braunbek [30] coils and geometries [31] can be used to obtain a large uniform magnetic field volume. The simplest arrangement to obtain a uniform magnetic field over a large volume is to get two identical coils which carry the same amount of current and place them the distance d apart from each other as shown in Figure 2.5a. For rectangular coils with the side lengths $2a$ and $2b$, this yields a rather lengthy expression given in Chapter A.

The magnetic field strength at $z = 0$ is an even function in z, i.e. all derivatives of odd order to z disappear, due to the symmetrical arrangement. The highest homogeneity is achieved if also the second order derivative in z vanishes [32]

$$\left.\frac{\mathrm{d}^2\vec{B}(z)}{\mathrm{d}z^2}\right|_{z=0} = \vec{0}\,. \tag{2.40}$$

Using this condition for a square coil pair with side length $2a$, the ideal distance d in which the coil pair should be placed for the highest uniformity can be given analytically as [33]

$$\frac{d}{2} = 0.5445a\,. \tag{2.41}$$

For a rectangular coil pair the resulting expression from evaluating Equation 2.40 can be computed numerically as a function of the ratio of both sides a and b and is depicted in Figure 2.6. Square coil pairs wich satisfy the condition in Equation 2.41 and rectangular coil pairs which satisfy the condition displayed in Figure 2.6 are called Helmholtz Coils.

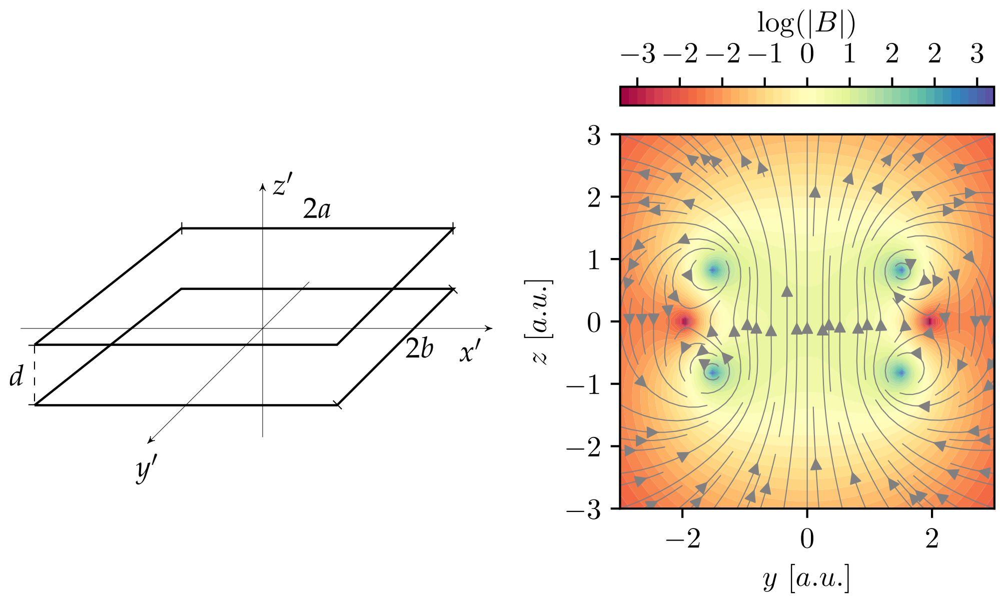

(a) **(b)**

Figure 2.5: (a) Schematic of a rectangular Helmholtz coil pair. The individual coils with side lengths $2a$ in x direction and $2b$ in y direction are placed the distance d along the z direction apart from each other. The axis trough the geometric center, here the z axis, is referred to as the central axis. **(b)** Exemplary magnetic field strength and vector character of the field produced by such an arrangement in the zy-plane placed at the ideal distance apart.

The magnetic field of a rectangular Helmholtz Coils on the z-axis is given as

$$\begin{aligned} B_z(z) = \frac{ab\mu_0 In}{\pi} \Bigg[& \frac{1}{\left(b^2 + \left(\frac{d}{2}+z\right)^2\right)\sqrt{a^2+b^2+\left(\frac{d}{2}+z\right)^2}} \\ & + \frac{1}{\left(b^2 + \left(\frac{d}{2}-z\right)^2\right)\sqrt{a^2+b^2+\left(\frac{d}{2}-z\right)^2}} \\ & + \frac{1}{\left(a^2 + \left(\frac{d}{2}+z\right)^2\right)\sqrt{a^2+b^2+\left(\frac{d}{2}+z\right)^2}} \\ & + \frac{1}{\left(a^2 + \left(\frac{d}{2}-z\right)^2\right)\sqrt{a^2+b^2+\left(\frac{d}{2}-z\right)^2}} \Bigg], \end{aligned} \tag{2.42}$$

with the number of turns n . In the center, where per construction only the z component survives, the magnitude is therefore

$$B_z(0,0,0) = \frac{2ab\mu_0 In}{\pi} \left[\frac{1}{\sqrt{a^2+b^2+(d/2)^2}} \left(\frac{1}{a^2+(d/2)^2} + \frac{1}{b^2+(d/2)^2} \right) \right]. \tag{2.43}$$

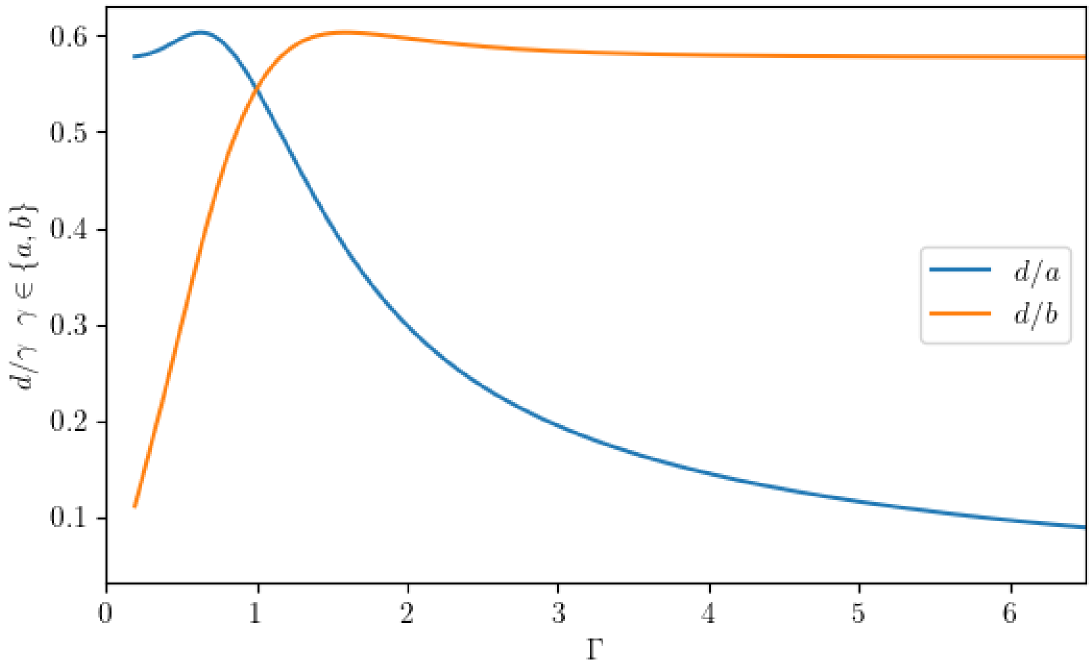

Figure 2.6: Ideal spacing d, normalized by the corresponding side lengths a and b respectively, to satisfy Equation 2.40 as a function of the ratio of the side lengths Γ of the coils.

In order to be able to estimate the uniformity, the deviation of the magnetic field magnitude from the center ΔB can be calculated as

$$\Delta B = \frac{|\vec{B}(x, y, z) - \vec{B}(0, 0, 0)|}{|\vec{B}(0, 0, 0)|}. \tag{2.44}$$

As a region with good uniformity $\Delta B \leq 0.1\%$ is assumed. This definition is made in order to have a target value for the coil design. The value of the threshold is set arbitrarily but small enough that it can be assumed that the magnetic field conditions at the cavity and at the magneto-optical trap, which are planned to be around 2 cm apart, are almost identical.

2.5 Time Variational Field

So far only the spatial dimension of the magnetic field has been discussed but as mentioned Maxwell's Equations also describe the time dynamics of the magnetic and electric field.

From Equation 2.21 it can be immediately seen that dynamic magnetic fields have an effect on the electric field. By using Stokes Law on Equation 2.21 [34] the expression

$$\oint_{\partial S} \vec{E} \cdot \mathrm{d}\vec{a} = \int_S \nabla \times \vec{E} \cdot \mathrm{d}\vec{S} \tag{2.45}$$

$$-\int_S \frac{\partial \vec{B}}{\partial t} \cdot \mathrm{d}\vec{S} = -\frac{\mathrm{d}}{\mathrm{d}t} \int_S \vec{B} \cdot \mathrm{d}\vec{S} = -\frac{\mathrm{d}\Phi}{\mathrm{d}t}, \tag{2.46}$$

is received, where Φ is the magnetic flux, defined as the amount of magnetic field passing through the surface of vector area $\vec{S}$. Changing the order of operation in Equation 2.46 is justified by Fubini's Theorem, see [35]. Performing the integration on the left side yields a potential difference, the induced voltage U_i

$$U_i = -\frac{\mathrm{d}\Phi}{\mathrm{d}t}. \tag{2.47}$$

In the case where the coil is stationary, only the current $I(t)$ can depend on time and therefore Equation 2.34 becomes

$$\begin{aligned} -\frac{\mathrm{d}\Phi}{\mathrm{d}t} &= -\frac{n\mu_0}{4\pi}\int_S\int \frac{1}{|\vec{r}-\vec{r}'|^2}\left(\frac{(\vec{r}-\vec{r}')}{|\vec{r}-\vec{r}'|^2}\times \mathrm{d}\vec{l}\right)\mathrm{d}\vec{S}\cdot\frac{\mathrm{d}I}{\mathrm{d}t} \\ &= -L_s\frac{\mathrm{d}I}{\mathrm{d}t}, \end{aligned} \tag{2.48}$$

where the purely geometrical proportionality factor L_s , called the self inductivity is defined. Because the magnetic field does also influence other arrangements than itself, in the same manner the mutual inductivity M is defined as

$$M_{ij} = \frac{\mu_0}{4\pi}\int_i\int_j \frac{\mathrm{d}\vec{l}_i\cdot\mathrm{d}\vec{l}_j}{|\vec{r}_i-\vec{r}_j|}. \tag{2.49}$$

There exist analytical solutions for Equation 2.48 and Equation 2.49 for rectangle geometries, but due to the unfeasible complexity of the computation there are also a variety of approximations that can be seen in [36–38]. The approximation used in this work focuses explicitly on Helmholtz coil arrangements and incorporates the physical extension of the coils. The overall inductance L is then given by [39]

$$L = 2L_s + 2M \tag{2.50}$$

$$\approx \frac{10^{-5}\cdot\zeta^2 n^2}{3\zeta+9\iota+10\gamma}, \tag{2.51}$$

where ζ denotes the effective side length, ι the coil width and γ the coil height, visualized in Figure 2.7b. With the induced voltage from Equation 2.47 and the equality from Equation 2.48, the behavior of a coil, described by its ohmic resistance R and its inductance L_s, in a circuit with time varying current is governed by Kirchhoffs law [40]

$$\begin{aligned} V(t) - (V_R + V_L) &= 0 \\ V(t) &= IR - L_s\frac{\mathrm{d}I}{\mathrm{d}t}, \end{aligned} \tag{2.52}$$

as depicted in Figure 2.7a. Solving this differential equation for the current $I(t)$ results in

$$I(t) = I_0\left(1-e^{-\frac{t}{\tau}}\right), \tag{2.53}$$

where the characteristic time constant

$$\tau = L/R, \tag{2.54}$$

of the system is defined. The circuit will settle to the new current value in about 5τ which is called the transient time. Due to $B \propto I$ this is also true for the magnetic field.

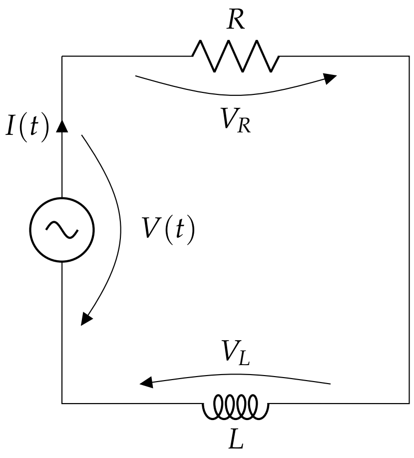

(a)

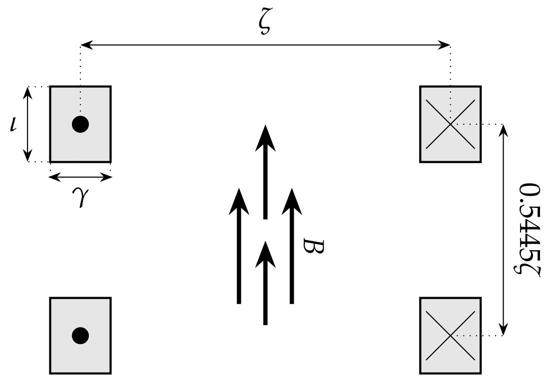

(b)

Figure 2.7: (a) Circuit diagram to describe the ohmic resistance R and the inductance L characteristic of a coil. Time variable current $I(t)$ and corresponding voltages V_i are shown. **(b)** Cross sectional view of square Helmholtz coil pair to illustrate the parameters ζ, ι and γ, used for the inductance approximation of the coil according to Equation 2.51 . Figure taken from [39].

2.6 Thermal Considerations

Although the experiment takes place at room temperature, additional heating, especially near the vacuum chamber, is not desired due to the sensitivity of the cavity. To get an estimation about the heating behaviour a plain model is derived.

The thermal characteristic of a current-carrying wire is made up of two main contributions. The dissipation of electrical power results in heating of the material, due to the Joule effect, whilst the heat convection with the surrounding cools the material, in its simplest form also known as Newton cooling [41]. The applied power P increases the inner energy U of the material, which loses this heat in a convective flow $\vec{j}_t$ through the oriented surface element $\mathrm{d}\vec{S}$ [42]

$$P = \frac{\mathrm{d}U}{\mathrm{d}t} + \oint \vec{j}_t \cdot \mathrm{d}\vec{S} \tag{2.55}$$

$$= m\alpha\frac{\mathrm{d}T}{\mathrm{d}t} + hS\Delta T, \tag{2.56}$$

where m denotes the mass, α the specific heat capacity of the material and h the heat transfer coefficient of the material at the interface. Solving this differential equation for the temperature difference ΔT between the surrounding and the surface temperature of the material, with the physical reasonable boundary condition $\Delta T(0) = 0\,\mathrm{K}$, yields

$$\begin{aligned} \Delta T &= -\frac{P}{hS}e^{-\frac{hS}{\alpha m}t} + \frac{P}{hS}, \\ \Delta T_{max} &= \frac{P}{hS}, \end{aligned} \tag{2.57}$$

with the maximal reached temperature difference ΔT_{max}.

With this rather simple model of the thermal behaviour an approximation about the surface temperature is possible.

3 Design and Implementation

After the theoretical foundations were set out in the previous chapter, this chapter is dedicated to the practical implementation of a first magnetic field coil. First, the objectives and constraints, given by the overall experiment, are presented. Then the design implementation and setup of a prototype is described.

3.1 Design Goals and Constrains

The design goals arise from different aspects of the experiment. On the one hand there are necessary demands from the physics side, like the compensation of earths magnetic field and the required field strength to reach for the splitting, as laid out in Section 2.1 and Section 2.2. These demands of the magnetic field strength differ for the different axis are in the range between 0.2 G and 1 G[1]. On the other hand there are more flexible conditions like the allowed power consumption and the way to integrate the coils into the experiment.

The need of a triaxial compensation system arises directly from Section 2.2 where the magnitude of each axis is also given by Equation 2.20. That a guiding field is required comes from the need to define the polarization according to the quantization axis this field provides. For most of the planned experiments there are no requirements on the strength of this guiding field. The guiding field should be small enough, so that still both of the used ground state sublevels couple to the cavity mode. On the other hand, a stronger guiding field results in lower fluctuations relative to the field amplitude which is desirable for the coherence time. Besides that, the Raman coupling procedure of the states benefits from a higher guiding field because this allows for the spectral differentiation of individual states. This enables the driving of individual selected states as described in [11]. Typical values for the guiding field to perform this procedure are at around 0.5 G [11]. The guiding field can be generated through the triaxial compensation system by providing a bias current on the coils responsible for the desired axis.

Constrains are mostly given by the position and dimension of other components of the experiment, such as the vacuum chamber where the optical cavity is embedded in, as well as the surrounding optics. To perform the desired experiments, it is necessary to interact with the atoms to trap, address and image them. Good optical access is therefore mandatory. The vacuum chamber must fit inside the compensation system without direct contact to avoid heat transfer, possible current leakage and shortcuts. At the same time the system must fit tight enough to allow the optical components to be placed as near as possible to the vacuum chamber. The homoge-

[1] Due to the variety of different units used to describe the magnetic field strength it should be mentioned that $1\,\mathrm{G} \mathrel{\widehat{=}} 0.1\,\mathrm{mT} \mathrel{\widehat{=}} 10^{-4}\,\mathrm{T}$.

neous volume of the generated magnetic field must include the whole cavity volume as well as the adjacent magneto-optical trap (MOT), around 2 cm apart in the y direction, with as little deviation as possible. The maximum achievable uniform volume directly depends on the coil side length, which is determined by the height of the cavity over the optical table. The height of the cavity above the table is freely selectable in principle. In order to have a modular design, the vacuum is placed at a breadboard on the laser table. Taking into account standard dimensions of metric optical posts and the susceptibility to vibrations, a height of 137.3 mm above the breadboard, where also the coils will be placed, is chosen for the position of the cavity.

As mentioned before, a concern is the heating of the system due to the dissipation of the input power. Due to the use of optics it was decided to not use forced air cooling. Also water cooling is ruled out on account of special circumstances with the available water cooling system and to minimize the possible points of failures. An additional requirement comes from how the experiment is driven. There will be two phases with different demands on the magnetic field, the loading and the experiment phase, so that the magnetic field will be varied in operation. From Section 2.5 it is obvious that the switching won't be instantaneous, so keeping the switching time in reasonable limits must also be regarded in the coil design.

To summarize, the design must generate a magnetic field high enough to compensate for background fields in each component, mainly due to earth's magnetic field whichs largest component is around 0.448 G. There must also be a margin for interference field from electrical components of the experiment. In addition to that, a guiding field must be able to be generated with at least 0.5 G. This field must be as uniform as possible and should extend at least to the MOT without loosing the uniformity, which compels to use three coil pairs. Some constrains on the maximal uniform volume achievable are given through the position of the cavity because this restricts the possible side length the coils can have. The passive cooling sets a limit to the current which can be applied, as can be seen from Equation 2.57[2] and the request to a reasonable switching time sets a demand on the number of turns, as shown in Equation 2.51.

3.2 Helmholtz Coil Design and Manufacturing

Due to the mentioned constrains, the implementation is not as straightforward as following step by step methods for the design of Helmholtz coils, as done for example in [39]. The various dependencies of the desired coil pair properties requires the optimization of various parameters simultaneously. The used parameters are the result of multiple consecutive iterations and are further presented in the following.

Design Implementation

Helmholtz coils, one pair for each spatial direction, will be used as magnetic field source due to several reasons. Firstly, Helmholtz coils generate a uniform field, the magnitude of which can be easily adjusted by selecting a suitable number of coil turns and varying the applied current. Secondly, they allow for good optical access into the vacuum chamber which is necessary for trapping, addressing and imaging

[2] Because of the quadratic relationship $P = I^2 R$ between the power P and the current I.

Table 3.1: Physical properties of the planned coil pairs. Side lengths, resulting ideal distance, relationship between the magnetic field strength in the center and the applied current and number of turns

Coil Pair	side	length [mm]	distance [mm]	B/I [G/A]	n
x	a	213.52	116.26	3.82	52
	b	253.52			
y	$a = b$	253.52	138.04	3.34	52
z	$a = b$	213.52	116.26	3.97	52

the atoms. Thirdly, they can be constructed modularly and with a small footprint, so that the whole assembly can be placed on the same breadboard as the vacuum chamber.

Rectangular Helmholtz coils are chosen over round ones due to the larger uniform field volume at comparable side length [32] and the absence of an additional mount for positioning. Two of the pairs are square and one is rectangular, to avoid collisions with the tube attached to the vacuum chamber, which connects to the vacuum pumps. The arrangement of the complete system is shown in Figure 3.1. The rectangular coil pair isn't placed in the ideal distance for its ratio, but instead at the distance which would be ideal for a square coil with side length of the shorter side, because this would partially block the optical access into the vacuum chamber. Despite the non-ideal spacing the uniform region of the magnetic field extends far enough as shown in Figure 3.2. Nevertheless, to ensure the structural integrity even without an additional mount each coil frame is constructed from U-shaped aluminium profiles. Aluminium is chosen because of its low magnetic susceptibility[3], ease to process and structural soundness. These frames also act as holding points where each other coil is fixed via custom designed aluminium clamps. For easier manufacturing and the possibility of analytical descriptions, three equal square coil pairs arranged in a sort of interwoven cage as in [44] would be preferable. But to meet the need for accessibility, the more flexible and accessible design as proposed here is chosen.

It is worth to note that this design fulfills the requirements planned as from the current stage of the experiment. In the future additional constrains and needs can arise, such as the necessity of active real time compensation of the magnetic field when higher coherence times are required.

As earlier mentioned, the side length to achieve the biggest uniform volume is determined by the cavity height and can be in theory two times these height. After subtracting material thickness and the thickness due to the coil turns the effective side lengths of all pairs are given in Table 3.1, together with the ideal distance between the coils, derived by Equation 2.41. These side lengths are measured in the center of the wire bundle and neglect the curvature at the end.

From here on the remaining parameters number of turns, applied current and magnetic field magnitude are heavily dependent on each other as apparent from Equation 2.43. The optimization of all these parameters must be done simultaneously. The chosen values for these parameters originate from the end of an iterative process and provide a balance on all mentioned aspects plus the physical size of the coil itself, the employed wire and manufacturability.

[3] The molar magnetic susceptibility of aluminum is $\chi_{\mathrm{m}}(\mathrm{AL}) = 4\pi \cdot 16.5 \times 10^{-6}\,\mathrm{cm}^3/\mathrm{mol}$ [43].

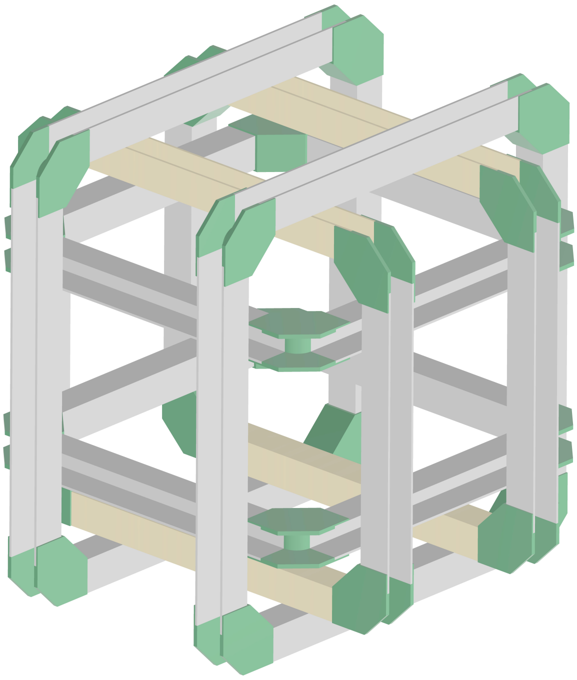

Figure 3.1: Illustration of the computer-aided design (CAD) of the planned compensation system. The L-connectors are shown in green. The X-connectors are not shown for visual clarity. From outer to inner there is the y-, the x- and the z-coil pair. Sand color shows the side b of the x-coil which is longer than the a side of the coil to avoid collisions with the vacuum chamber plumping.

A useful quantity to describe coils is the magnetic field amplitude that they can generate for an applied current. A value of $B/I = 3.33\,\mathrm{G/A}$ is obtained if the operating current is chosen to be around 300 mA while aiming for a magnetic field strength of 1 G. The low current value is chosen to keep the heating minimal while the value for the magnetic field strength is motivated as described in Section 3.1. To reach this B/I value the number of turns must be $n = 52$.

The exact B/I values for each coil pair are given in Table 3.1. The wire[4] was chosen to be a round, precoated copper wire with the largest diameter[5] possible to be bend and fit into standard aluminium U-profiles.

Using orthocycling winding [45], as shown in Figure 3.3, to obtain a nearly square cross section of the coil, the coil width w and the coil height h are calculated to be

$$\begin{aligned} w &= (q+0.5)\,d = (8+0.5)\cdot 2\,\mathrm{mm} = 17.00\,\mathrm{mm} \\ h &= \left(1+\frac{\sqrt{3}}{2}\,(p+1)\right) d = \left(1+\frac{\sqrt{3}}{2}(7+1)\right)\cdot 2\,\mathrm{mm} = 15.86\,\mathrm{mm} \end{aligned} \tag{3.1}$$

[4]SchneiTec: Kupferlackdraht W210, 2mm, rund.

[5]Because the heating depends on the Power $P = I^2R$ and the resistance R on the diameter of the wire $R = \varrho l/A$ with the specific resistivity of copper , the length of the wire l and the cross sectional area A which itself depends on the diameter d_w of the wire. So additionally to using a low current, the resistance should be low as well to minimize the heating.

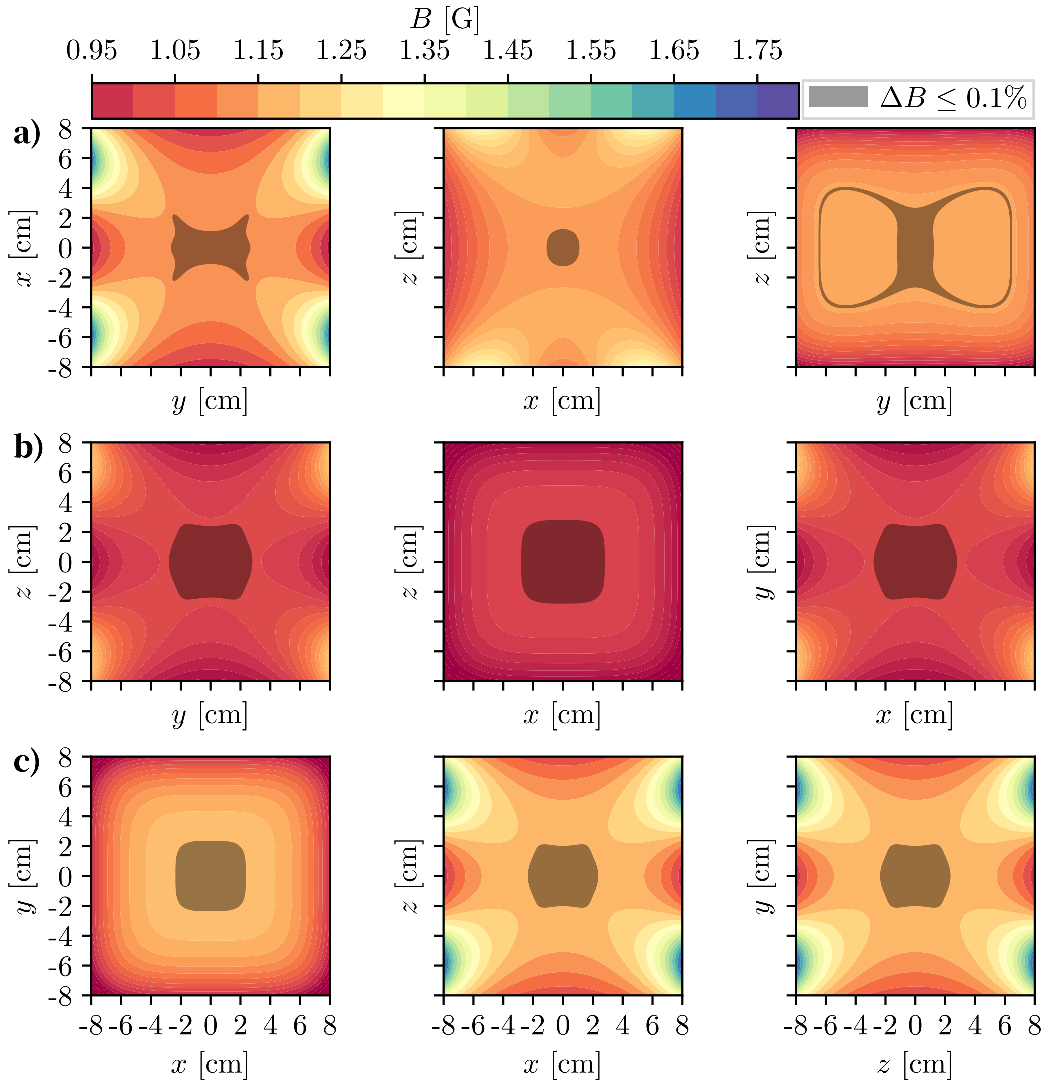

Figure 3.2: Magnetic field amplitude in the respective plane of the designed Helmholtz coil pairs, the x coil pair shown in **a)** and the y and z pairs in **b)** respectively **c)**. The dark shaded region shows the area where the deviation of the magnetic field amplitude is less or equal than 0.1% of the amplitude in the center. All regions in the xy plane extent far enough to encompass the position of the MOT, planned to be 2 cm away from the center in the y direction. The extent in the x direction is also sufficient, due to the submillimeter spacing of the cavity.

with the diameter of the wire $d_w = 2\,\mathrm{mm}$, the number of layers $p = 7$ and strains of wire in each layer $q = 8$. This fits into a standard $20\,\mathrm{mm} \times 20\,\mathrm{mm}$ aluminium profile[6], which has a wall thickness of 1.5 mm.

The connections between the aluminum parts are 3D printed from Polyactide (PLA),[7] this material and manufacturing method was chosen due to the low mag-

[6]Alberts: Art.-Nr. 473877, U-Profil Aluminium.

[7]It should be noted that the final L-connectors are better made out of aluminium as well because PLA has the potential to inflame if hit accidentally by higher laser power outputs. Here attention must

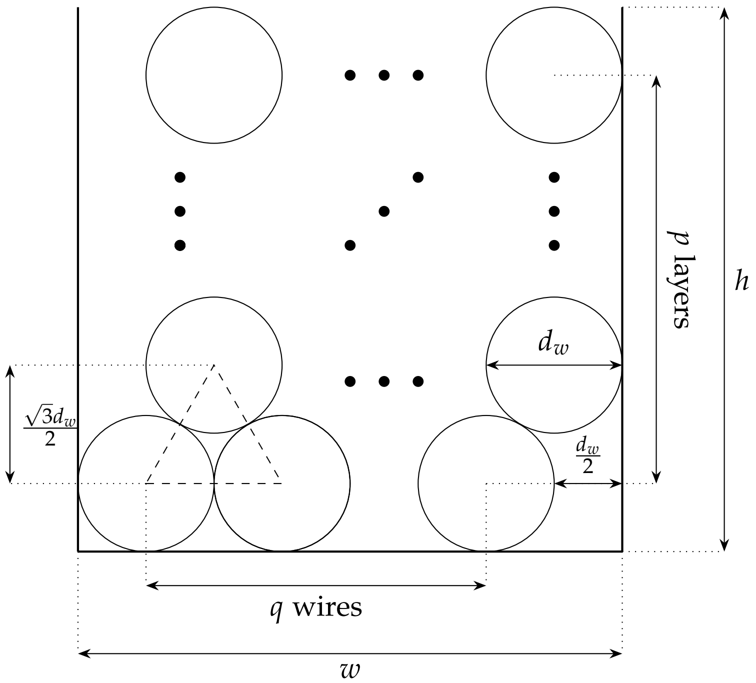

Figure 3.3: Schematic of an orthocycling winding, with number of wires q in each layer p. The coil width w only depends on the used wire diameter d_w when there are the same number of wires in each layer. The coil height h can be obtained by using the height of the equilateral as depicted.

netic susceptibility, sturdiness and rapid development cycle. Improvements to the design could be tested in just a few minutes as a 3D printer[8] was available at the institute. These L-connectors, named due to their shape, are designed with a radius of curvature of 1 cm so that the wire can bend without the risk of damaging the isolation coating. For each coil there is one L-connector with an inlet and an outlet hole in the walls to route the wire in and out of the frame. All blueprints of the mentioned components are shown in Chapter B. To align, stabilize and fasten each coil, custom aluminium clamps, called X-connectors due to their shape, are constructed. To secure the whole arrangement on the laser table simple aluminium bars with a slot down the center line are intended. The fixation on to the laser table is necessary as long the whole arrangement isn't fully assembled.

Prototype Manufacturing

In order to verify the intended design's features, a single coil pair is produced and its performance are evaluated. As a first prototype, the z-pair is chosen because they are the smallest coils and therefore have the lowest production costs.

Additionally to the coil pair itself, a wooden cross structure is made where the coil can be fixed during the winding process. This wooden cross has a hole in the center to mount a threaded stand which itself can be chucked into a vice. The threaded stand acts as an rotary axis during the coil windig.

be paid to possible occurring eddy currents. This could be prevented by adding an electrical isolation layer between the L-connectors and the U-profiles.

[8] Bambu Lab X1C

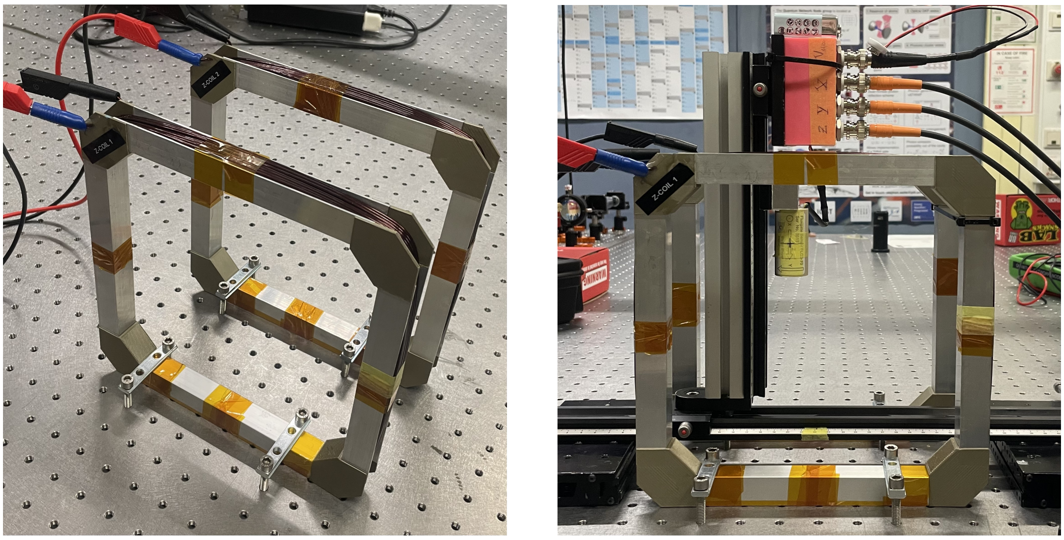

(a) **(b)**

Figure 3.4: (a) Picture of the built z coil pair prototype fixed on the laser table and connected to the power supply. This assembly doesn't correct for the relative vertical tilt and is therefore only used for the heating measurement. **(b)** Assembly to measure the magnetic field in the plane between the coil pair. The fluxgate is mounted onto a rail system, capable to move in the x and y direction. A cable tie on the upper right corner of the coil pair corrects the tilt of the arrangement. The pink box houses the electrical connections from the fluxgate and provides four BNC connectors, one for the battery and three for the data output which are connected to an oscilloscope. The Kapton tape protects the areas where the wire the most exposed and therefore susceptible to scratches.

The ends of the trimmed aluminium profiles are first degreased with isopropanol and then glued into the L-connectors with superglue such that a rigid frame is made. This initial fixation is necessary so that the frame can withstand the forces of winding the first coil layer, the firmness in the end comes from the tension the wire exerts on the frame and not from the glued connections. The frame is clamped at all four corners onto the wooden cross and the wire is routed through the input hole and secured in place by a cable stop. For the wire routing, attention must be paid on the direction in which the frame is turned. While winding the coil it is important to keep the wire under tension at all times. This works best if the winding is done by two persons, one providing resistance at the wire spool while the other one is rotating the frame against the resistance.

To obtain an evenly wound coil the first layer is especially important. Here, the person who rotates the frame must keep an eye that each wire strain is laid down straight and close to the previous strain. To minimize the deformation of the wire it should not be pulled by hand but only by the rotation of the frame while gently guided by adjusting the position of the cable drum and the frame to each other. Once one cable segment is deformed it is nearly impossible to get it as straight as from the factory again, and therefore introducing deviations in the winding pattern. Each layer after the first one is laid into the groove between the cables of the previous layer. It happens that when going over the corner the wire may jump out of the groove into the subsequent one. This becomes noticeable by a drop of the tension and an audible metallic sound, like pulling a guitar string. In this case, the winding must be returned to the point at which the winding pattern was still maintained and a new start must be made from there, keeping the tension in the wire.

The initial plan for the winding pattern was to go with seven layers with eight strains in each layer. It turns out that an alternating sequence of eight and seven strains gives a more uniform result while having the same dimensions. This pattern is more forgetful regarding the imperfections of the wire which are mainly due to smallest deformations and residual stress in the wire itself.

Once the number of turns is met, the wire is routed through the output hole of the L-connector and is secured with an cable stop. Now, the wire is glued in place at both the input and output holes. Additionally, a larger area on the outer side of the connector is also covered with glue to maximize the surface area that the adhesive can act upon.

A two-component epoxy is used for this to withstand the forces the wire exerts on these places once the cable stops are removed. The epoxy was also chosen for its heat resistance because the wire transfers a lot of heat during the soldering process. After the epoxy cured the costing of the wire ends is removed and the electrical connections are soldered on. For the electrical connections 4 mm banana sockets[9] are selected, these provide a standard interface for the power supply and measuring devices. The so constructed prototype, shown in Figure 3.4a, differs from the planned version mainly in the cross sectional height of the wire bundle. As more layers are added onto the coil the more it morphs to a round shape. This effect leads to the height, in Equation 3.1 calculated as of $h = 15.86\,\mathrm{mm}$, exceeding by roughly 4 mm at the highest part of the coil.

[9] RS: RS PRO 4 mm Bananenbuchse, Art.-Nr.45515-7-109-3-BL.

4 Characterization

In this chapter, the properties of the prototype are tested with regard to the previously mentioned requirements such as field strength and homogeneity. Various parameters of the magnetic field produced by the coils, as well as the response time of the system and the heating during the operation of the coils are analysed.

Although the prototype built is the z coil pair, the coils are placed with their symmetry plane perpendicular to the laser table, as shown in Figure 3.4a. This is due to a simpler assembly as long as there is only one coil pair, otherwise an additional scaffold would have had to be built. With this setup there is still a minor tilt perpendicular to the table surface, which is corrected with cable ties on the upper part of the coils. When the whole system is arranged the cable ties are not needed anymore because the coils are fixed to each other. The coordinate system used in the measurements is similar to the one shown in Figure 2.5a just rotated 90° around the x axis. In this orientation the magnetic field points along the z axis.

During all of the characterization measurements the power supply unit DW Instek GPS-1850D is used to power the coils. In the later experimental setup an ultra low noise, long term stable power supply unit should be used to minimize possible fluctuations in the magnetic field induced by fluctuating current.

4.1 Magnetic Field Characterization

This section shows the performance of the coils in generating a magnetic field with desired strength at a given input current, as well as the magnetic field strength at the central axis of the arrangement and the uniformity in the plane between the coils. To sense the magnetic field a triaxial fluxgate[1] is employed. The output of the fluxgate is measured by an oscilloscope[2]. Due to the size of the fluxgate the actual position of sensing must be found. For this the fluxgate is placed on the table and a permanent magnet is passed by parallel to each axis in sufficient distance. The field progression is observed on the oscilloscope and when the turning point occurs the, position is marked on the fluxgate. With this procedure the sensing area is determined to be in the geometric center of the fluxgate.

The measurement error of this setup is the sum of the error on the oscilloscope, estimated to be $\pm 5\,\mathrm{mV}$, and the fluxgate, which itself is composed of an static factor of $\pm 5\,\mu\mathrm{T}$ and a dynamic part of $\pm 1\%$ of the measured value.

[1]Stefan Mayer Instruments FLC3-70 [46]
[2]Rigol DS1054Z

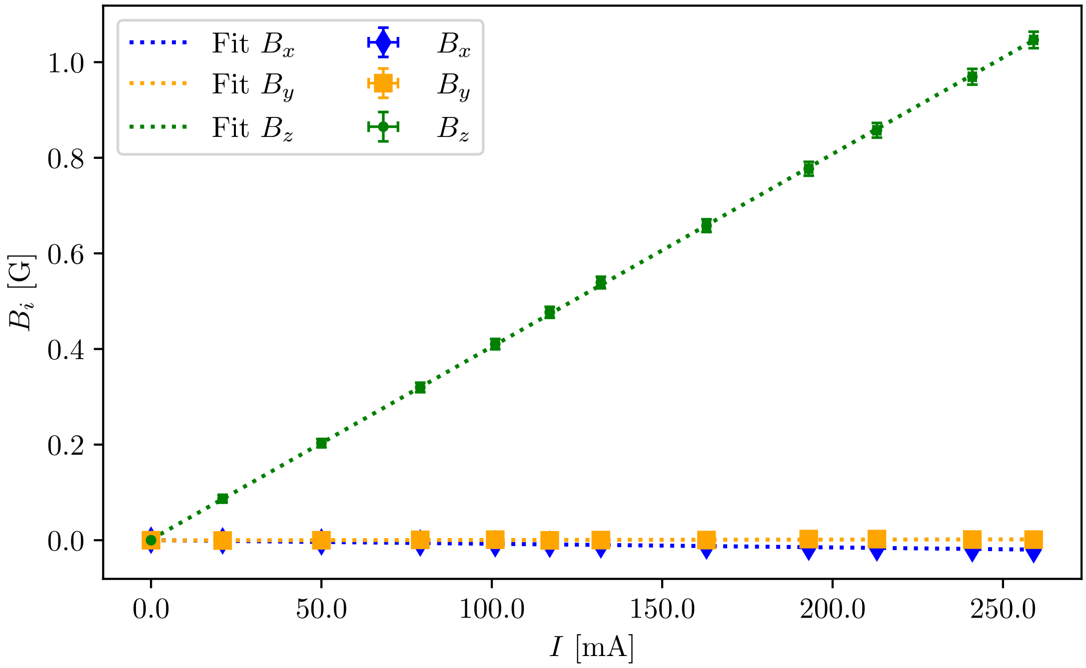

Figure 4.1: Magnetic field magnitude of each component B_i at the center $(0, 0, 0)$ for varying currents I supplied to the coil pair. A strong dependence of the B_z component on I can be seen, while both other components show only a slight change with rising current. The linear relationship between the magnetic field strength of each component and the current is used to obtain B_i/I values via a fit to the data. The obtained values are reported, together with the expected values from the theory, in Table 4.1.

Magnetic Field as Function of the Applied Current

To evaluate the expected linear relationship between the magnetic field strength B and the input current I on the coil pair, as stated in Equation 2.43, the field strength in the center is measured with a fluxgate for various input currents. The triaxial fluxgate is used so that also the cross-talk between the components can be assessed directly. The input current provided by the power supply, is varied between 0 mA and 259 mA, where the upper limit is given by the fluxgate[3].

The measured values are corrected about their respective offset $B_i(0\,\mathrm{mA})$, determined by the background field, and are depicted in Figure 4.1. Here the error in the set current $\Delta I = \pm 1\,\mathrm{mA}$ is an estimation on the precision of the used power supply whereas the measurement error of the magnetic field strength is composed as described earlier. To estimate the B/I values and to compare them to the theoretical values a linear function $y = mx + b$ is fitted to the data, where the slope m corresponds to B_i/I. The obtained $(B_i/I)_\mathrm{m}$ values are shown in Table 4.1 with their respective error $\Delta(B_i/I)_\mathrm{m}$ and the theoretical values $(B_i/I)_\mathrm{t}$.

As evident from Figure 4.1, the linear B/I relationship is measured and is with (4.032 ± 0.009) G slightly higher than the expected 3.97 G. Despite the deviation of about 1.6% this is in agreement with the theory. The deviation is most likely due to

[3]To prevent damaging the sensor and to suppress noise in the measuring signal, the fluxgate is operated with a 9 V battery. This restricts the measuring range to about ± 1.5 G.

Table 4.1: Overview of the calculated $(B_i/I)_t$ and measured $(B_i/I)_m$ relationship between the magnetic field and the applied current for each component of the build prototype. The error is obtained by the entries of the covariance matrix of the performed fit as shown in Figure 4.1

Component	$(B_i/I)_t$ [G/A]	$(B_i/I)_m$ [G/A]
B_x	0.00	0.076 ±0.001
B_y	0.00	0.008 ±0.003
B_z	3.97	4.032 ±0.009

the spatial extent of the coils which is not taken into account in the model. The x and y components of the magnetic field show only very small B/I values. For the planned operating current range used in the experiment this would translate into a maximum additional magnetic field of 0.03 G in the x direction and 0.001 G in the y direction. From the calculations there shouldn't be, by construction, any magnitude at all in this components. This cross talk arises presumably from the, unavoidable not perfect, relative placement of the coils. The coils are most likely not placed perfectly square to each other. An additional source of can be the alignment of the fluxgate. Despite the unwantedness of this cross talk this shouldn't be a problem when the entire system, composed of one coil pair for each direction, is on operation. On the one hand the relative placement of the coils can be done much more precise because more mounting points are available. On the other hand it should be possible to compensate for this low magnitudes with the other coil pairs.

Magnetic Field along Central Axis

To evaluate the magnetic field along the symmetry axis of the arrangement a data point is taken every centimeter in a range of 40 cm along the central axis. Each data point contains two measurements: first the background magnetic field component is measured while the coil pair is not powered on, and second the magnetic field component is measured again with powered coils. The powered value is corrected about the background measurement and plotted in Figure 4.2. The error in the positioning of the fluxgate Δz is estimated to be 1 mm whereas the error of the magnetic field strength is obtained as described earlier. Powering the coils was only possible with 150 mA because at higher currents the measurement range of the fluxgate were exceeded due to a high background field. With the results of Section 4.1 the findings can be extrapolated to the planned current operation range.

Figure 4.2 shows the expected magnetic field profile produced by a set of square Helmholtz coils. The measured magnetic field profile agrees well with the theoretical profile in the regions far away from the center. Progressing towards the central region the measured magnitudes all lie above the predictions, which agrees with the findings for the B_z/I value in Section 4.1. As depicted in the inset of Figure 4.2, the region ±2 cm around the center is, as expected, highly uniform.

Magnetic Field in the Plane

To obtain an deeper insight on the uniformity of the field in the central region perpendicular to the axis measured in Section 4.1 the magnitude of the magnetic field throughout the plane between both coils is measured.

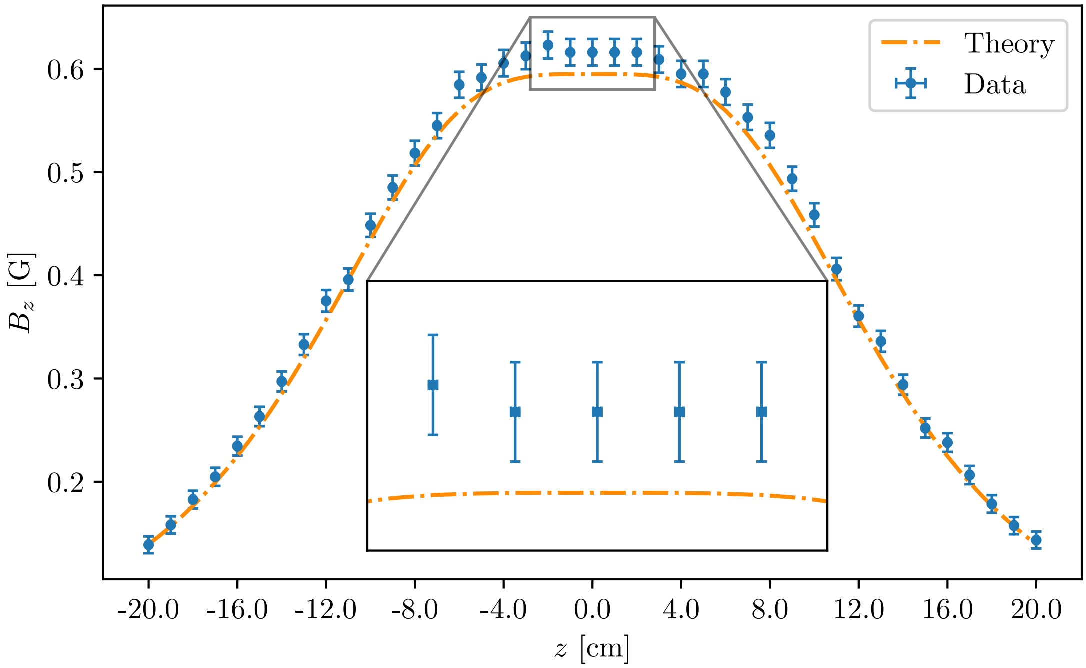

Figure 4.2: Amplitude of the B_z component at varying position z on the central axis. The measurement is taken with current $I = 150\,\text{mA}$ supplied to the coil pair. The profile matches the theoretical prediction in general shape, only in the center the amplitude is slightly higher than predicted wich originates from the spatial extend of the physical coils. The central region at $2\,\text{cm} \times 2\,\text{cm}$ shows, as expected, high uniformity.

For a region of $5\,\text{cm} \times 5\,\text{cm}$ around the center all components of the magnetic field are measured. Every centimeter a background measurement and immediately after that a measurement with powered coils at $I = 200\,\text{mA}$ is taken. Each component is corrected about its offset and the absolut value is calculated. The absolut values are shown in Figure 4.3a.

The magnetic field strength is, as noted in the previous measurements, higher than calculated. At the center the measured strength is $B_m(0,0) = 0.859\,\text{G}$ whereas the calculated values is $B_t(0,0) = 0.794\,\text{G}$. This discrepancy of around 8% arises from the cross-talk of the other components as well as from the general higher B/I value of the coil, as shown in Section 4.1.

The upper area of the measured region shows the expected behavior of decreasing amplitude the further away from the center. The lower part follows this trend in the y direction but not in the x direction. Here the amplitude starts to increase the further away from the center. In the measured region there is therefore a gradient in the x direction. This behavior probably comes from the table top of the laser table which is magnetizable as an examination with a permanent magnet shows. For testing this hypothesis and ruling out any contributions to this behavior of the coils itself, the same measurement should be repeated with an non magnetic surface as a table top.

The standard deviation of the magnetic field amplitude in the region of particular interest, $2\,\text{cm} \times 2\,\text{cm}$ around the center, is about $0.010\,\text{G}$ which is about 1.19% of the

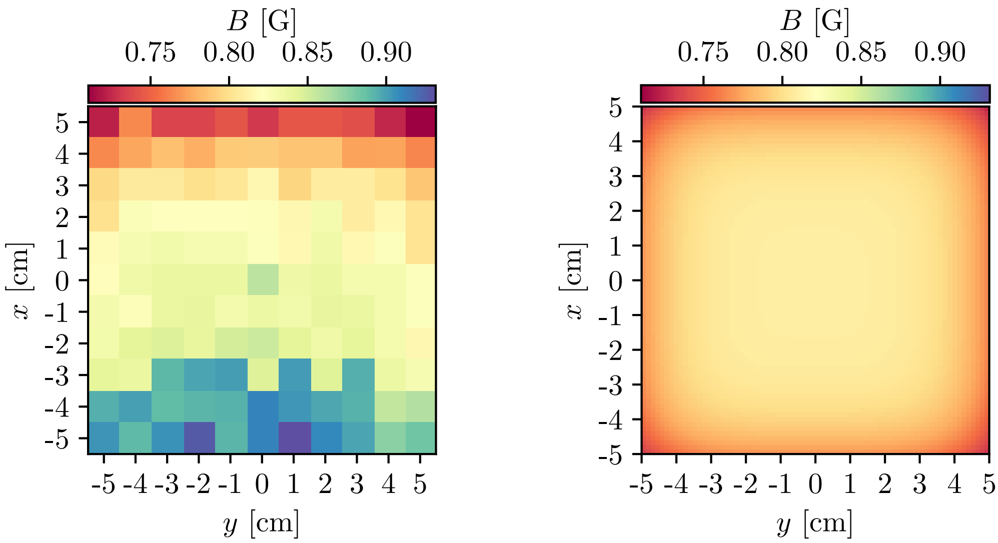

(a) **(b)**

Figure 4.3: (a) Magnetic field amplitude B of the z coil pair in the xy plane at supplied current $I = 200\,\text{mA}$. The upper half shows the expected behavior of concentric decreasing amplitude farther away from the center. The lower half shows a strong gradient of increasing amplitude in the x direction, which is not predicted by the theory. However, the amplitude progression of the lower half in the y direction, decreasing from the center line outwards, is again in line with prediction. The reason for this anomaly is most likely due to the interaction with the table where the coils pair is placed, since this material shows magnetic properties. **(b)** Simulation of the magnetic field in the xy plane produced by the z coil at $I = 200\,\text{mA}$.

mean value of this region.

This result confirms that the magnetic field produced by the coil pair is indeed highly uniform, not only on the central axis but also in the plane perpendicular to it.

4.2 Response Time

The response time of the coil pair is analyzed in two ways. One way is done by exploiting Equation 2.54, therefore measuring the resistance and inductance of the arrangement and calculating the response time τ^s directly. The second way consists of providing an rectangular voltage to the coils and measuring the induced voltage. Here the response time is obtained by the time course of the voltage, as described in Equation 2.52, and is further referred to as τ^d.

The inductance and the resistance of the whole arrangement as well as for each coil individually is measured with an LRC-meter[4]. The measured values are reported in Table 4.2 together with the calculated values, the resulting response time as well as the error. The error is calculated by estimating the maximum error of the LCR-meter as $\Delta R = 1\,\text{m}\Omega$ and $\Delta L = 1\,\mu\text{H}$ and using error propagation on Equation 2.54.

[4] Agilent E4980A

Table 4.2: Measured R and calculated R_t values of the resistance for each individual coil and the coil pair. Measured L and from Equation 2.51 calculated L_t values of the inductance for each coil and the coil pair. The coil pair is placed at Helmholtz configuration and is wired in series. The response time τ_t is calculated, according to Equation 2.54, from R_t and L_t. The value for the response time τ^s is calculated directly by the same equation using the measured values R_m and L_m. The error here propagates from the estimated precision of the LCR-meter. The value for the response time τ^d is obtained by fitting a function the form of Equation 2.53 on to the measured voltage profile seen in Figure 4.4. The error comes from the covariance matrix of the fit parameters.

Coil	R [mΩ]	R_t [mΩ]	L [mH]	L_t [mH]	τ_t [ms]	τ^s [ms]	τ^d [μs]
1	333	243.72	1.298	1.309	5.35	3.99 ±0.01	25.16 ±0.06
2	325	243.72	1.307	1.309	5.35	4.03 ±0.02	25.44 ±0.07
Pair	660	487.44	2.911	2.627	5.37	4.41 ±0.03	58.99 ±0.14

The measured and calculated resistance values differ from each other, wich is mainly due to the soldering points and the banana sockets. Additionally there is certainly a bit more wire used, due to the way it bends and the stacking, than in the naive calculation which takes just the side lengths and the number of winding into account. As in Table 4.2 apparent this difference is the reason for the deviation between the theoretical calculated response time τ and the response time calculated from the measured values. The approximation of the inductance, given by Equation 2.51 met the measured values in good agreement.

For the measurement where the rectangular voltage is applied a low frequency of 11 Hz is chosen, generated by an signal generator[5]. A sufficiently low frequency is mandatory to suppress possible alternating current effects. Due to the voltage induced by the coils at every change in the applied signal a voltage peak with exponential decaying outgoing flank is observed. The voltage profile is recorded by an oscilloscope and the response time is obtained by a fit of this data in the form of Equation 2.53[6]. This is done for the coil pair spaced apart in the ideal distance, as well as for each coil individually. The measured voltage profile and the corresponding fits are shown in Figure 4.4. The so obtained response times, and errors of the same, obtained by the covariance matrix of the fitting parameters, are reported in Table 4.2. The response times differs by a factor of 100 from the theoretical values as well as from the values of the other measurement.

To rule out any sources of error, this measurement was taken several times with different devices and different methods to obtain the voltage. One such verification measurement uses a current probe which itself produces an induced voltage when a changing magnetic field flows through it. The values of the response times where estimated by observing the oscilloscope output directly. A second approach used the proportionality of the magnetic field and the coil current. Here, an rectangular current signal of 30 Hz was applied to the coils and the time course of the magnetic field was measured with the fluxgate. The response time was obtained through the same fitting procedure as stated above. Each of the measurements verified the

[5] Thulby Thandar TG210.

[6] Where the proportionality $U = RI$ is used.

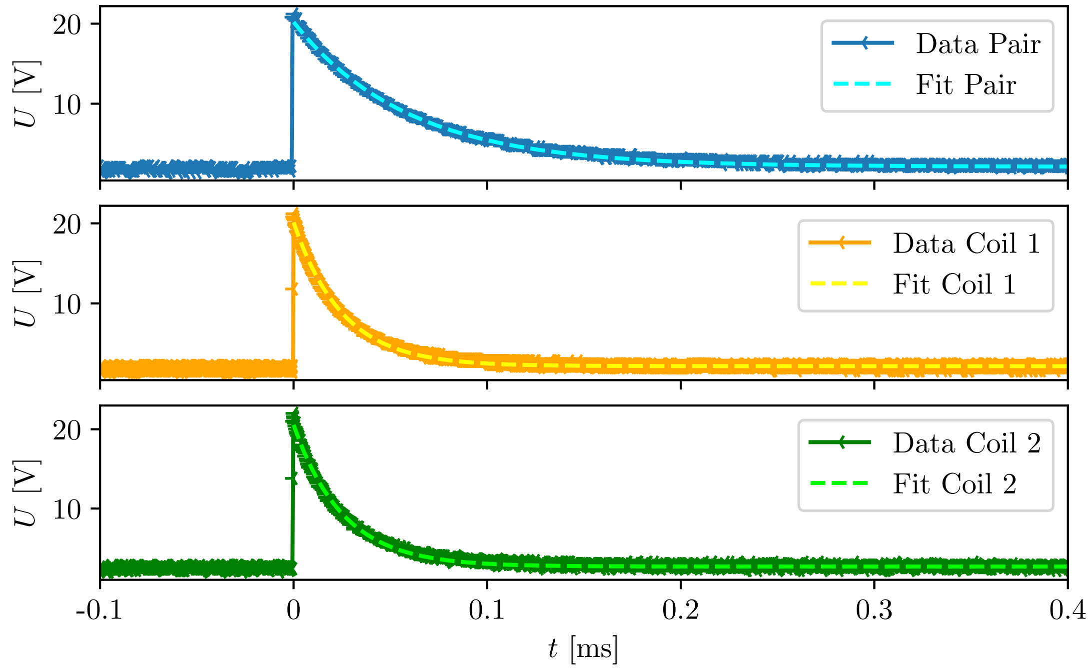

Figure 4.4: Recorded voltage profile of the individual coils and the coil pair with an applied signal of 11 Hz The peak in voltage peak is clearly visible as well as the exponential decay. Both curves of the individual coils run similar, while the curve of the coil pair decays slower. The exponential decay is described by the response time which is obtained by fitting a function of the form Equation 2.53 to the measured data. All obtained values for the response time are listed in Table 4.2.

order of magnitude of the stated value. This indicates that the theory described in Section 2.5 can not be used to describe the response time of the coils.

4.3 Heating Characterization

To estimate the thermal profile, the temperature of the powered coil pair is measured using a thermocouple connected to a handheld multimeter[7]. The ambient temperature is monitored by using a standard room thermometer. Every 15 s both temperatures are noted until several consecutive measurements no longer change. The input currents at which measurements take place are much higher than the planned operational range because measurable heating effects could only be observed for $I > 1\,\mathrm{A}$. The so recorded data is corrected about the systematic difference of both thermometers and is displayed in Figure 4.5.

To compare the logged data with the theory, as laid out in Section 2.6 some simplification must be made. To calculate the surface area of both coils the coil is approximated as solid copper pieces with smooth surfaces with height and width as derived in Equation 3.1 and with side length as tabulated in Table 3.1. The masses of these approximated coils are then obtained by multiplying the density of cooper[8] by the volume, the aluminium profiles are not taken into account. This approxi-

[7]Voltcraft M-4660A

[8]Density of cooper $\rho_{\mathrm{Cu}} = 8920\,\mathrm{kg/m^3}$ [43].

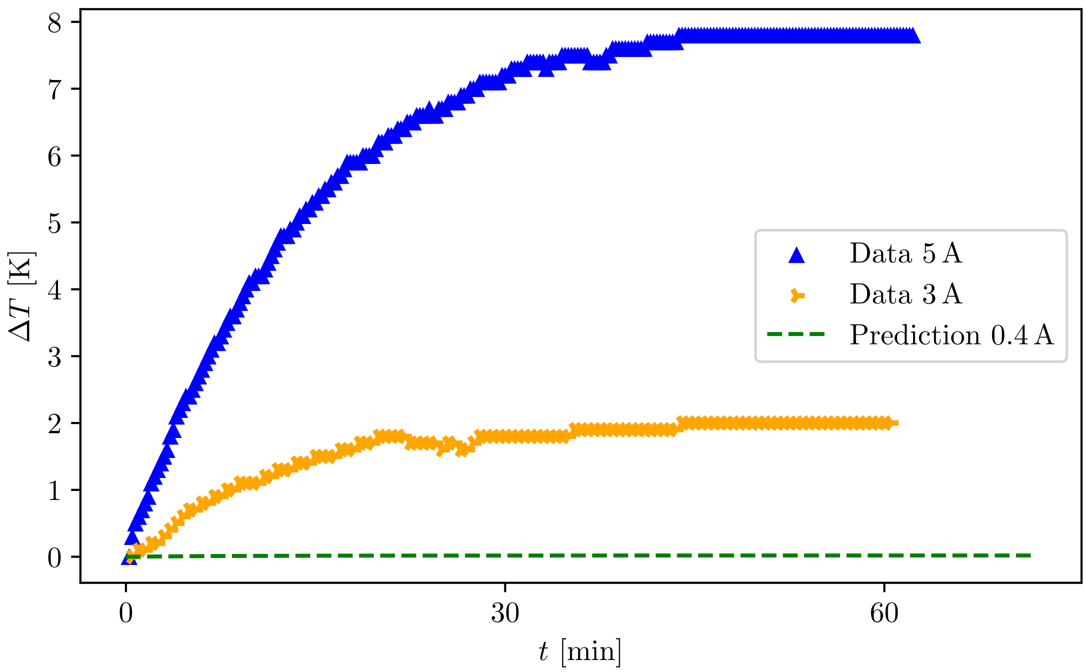

Figure 4.5: Time series of the temperature difference ΔT between the coil surface and the surrounding air. The general progression matches the theory as given in Equation 2.57. The heat transfer coefficients h obtained of both measurements are $18.55\,\mathrm{W/(m^2\,K)}$ and $27.66\,\mathrm{W/(m^2\,K)}$. Based on the lower h value the prediction shows practically no temperature raise for the upper limit of the planned current range at 0.4 mA one can see by the basically flat curve near zero.

mation overestimates the mass and underestimates the surface area by disregarding the interspaces between the wire strains. Also the heat transfer between the copper and the isolation and the isolation and the aluminium are neglected. Without these approximations an analysis would be to complex and would require the use of expensive simulation software. The specific heat capacity of cooper[9] is precisely known unlike the heat transfer coefficient of the surrounding air, which cannot be calculated easily due to its dependence on hard to access quantities [47]. This is also reflected in the literature values wich range from $5\,\mathrm{W/(m^2\,K)}$ to $25\,\mathrm{W/(m^2\,K)}$ for free convection in air and $25\,\mathrm{W/(m^2\,K)}$ to $250\,\mathrm{W/(m^2\,K)}$ for forced convection in air [48].

To obtain a realistic value for the heat transfer coefficient h a function of the form of Equation 2.57 is fitted to both measurements with the heat transfer coefficient as only fit parameter. The obtained values are $27.66\,\mathrm{W/(m^2\,K)}$ for the measurement at 3 A and $18.55\,\mathrm{W/(m^2\,K)}$ for the measurement at 5 A. The lower value is in the range of the literature values for free air convection, while the higher value lies slightly above more in the regime of forced air convection. Possible sources which forces the air to move during the measurement are the air conditioning units, opening and closing doors and moving people in the laboratory.

As from Figure 4.5 can be seen, the general form of the time series matches the theoretical prediction well. For the measurement at 5 A the maximum reached

[9] Specific heat capacity of cooper $\alpha_{\mathrm{CU}} = 385\,\mathrm{J/(kg\,K)}$ [43].

temperature difference to the surrounding was $\Delta T = 7.8\,°C$, while at $I = 3\,A$ the maximum temperature difference reached $\Delta T = 2.0\,°C$. Besides that, both measurements show that the system thermalizes after around 45 min, independent of the amount of current. Even with the many approximations made, the model is suitable to describe the system in good approximation.

The lower one of the obtained h value is used for a prediction of the thermal behavior at $I = 400\,mA$, the maximum planned operating current and is depicted in Figure 4.5. This results in a maximum temperature difference of 0.02 °C. This shows, that for the planned current range, the heat development will have practically no influence on the experiment.

5 Summary and Outlook

Summary

In this thesis, a triaxial magnetic field compensation system for the use in a quantum network experiment was designed and a prototype coil pair was built.

The arrangement was designed to address each spatial direction individually, to compensate for background fields and to provide a guiding field which defines a quantization axis for the atoms as well a reference axis for the photon polarization. Simulations of the magnetic fields were done to determine the extent of the homogeneous magnetic field volume for each coil pair. A first prototype was built out of commercially available aluminium profiles, copper wire and custom designed, 3D printed L-connectors.

Important characteristics were examined such as various properties of the magnetic field, the response time and the heating behaviour.

The magnetic field strength of each component as function of the applied current was measured and lies for the B_z component with (4.032 ± 0.009) G about 1.6% higher than the calculated value. The reason for the deviation presumably lies in the spatial extent of the real coils. This measurement also confirmed the low cross-talk in the other components.

A measurement of the magnetic field on the central axis was conducted. This showed high agreement with the expected magnetic field profile and a high uniformity in the central region along the axis.

The magnetic field in the plane between the coils was measured $5\,\mathrm{cm} \times 5\,\mathrm{cm}$ around the origin. Here, the standard deviation of the magnetic field strength at the most central region, $2\,\mathrm{cm} \times 2\,\mathrm{cm}$ around the origin, could be determined to 0.010 G, corresponding to about 1.19% of the mean value in this region. Apart from that an unexpected magnetic field gradient in the vertical direction was measured. This gradient likely comes from the magnetizable table top on which the coils were placed.

The response time of both individual coils and the coil pair was determined through calculation based on physical properties and a direct measurement. While the response times from the calculations are in agreement with the theory, the results from the direct measurement differ by an order of magnitude. This indicates that the used theory can't be used to describe the switching behaviour of the coils.

The temperature profile of the powered coils were recorded. For the planned operating current range of 300 mA to 400 mA, no measurable temperature raise could be observed. At currents above 1 A the qualitative course of the temperature curves is consistent with the model. Only the maximum temperatures are slightly below the predicted values.

Outlook

To verify the origin of the magnetic field gradient, as observed in the plane between the coil pair, the measurement of the magnetic field in the plane will be redone with an non-magnetizable mounting surface. Also an investigation into why the used theory for the response time fails to describe the observed behavior will be conducted.

In order to be able to use the proposed system as intended, the x and y coil pairs must be built and the entire arrangement assembled. Then the structural integrity, especially the contact points between the coils, and the possibility of precise placement can be assessed. Considerations on integrating the electrical connections into the L-connector are worth doing, to minimize the risk of breaking the in the current design very exposed banana sockets.

The examinations on the magnetic field properties should be done in the final configuration to verify the calculated values as well as to find the appropriate current settings for canceling out earth's magnetic field. In the bit more distant future, when the first goals of the experiment have been achieved, it must be assessed if active magnetic field stabilization is required to obtain higher coherence times. And if so, whether the here presented design is upgraded, complemented with an additional system or replaced entirely.

The system presented in this thesis is shown in Figure 5.1 together with the preliminary design of the vacuum chamber.

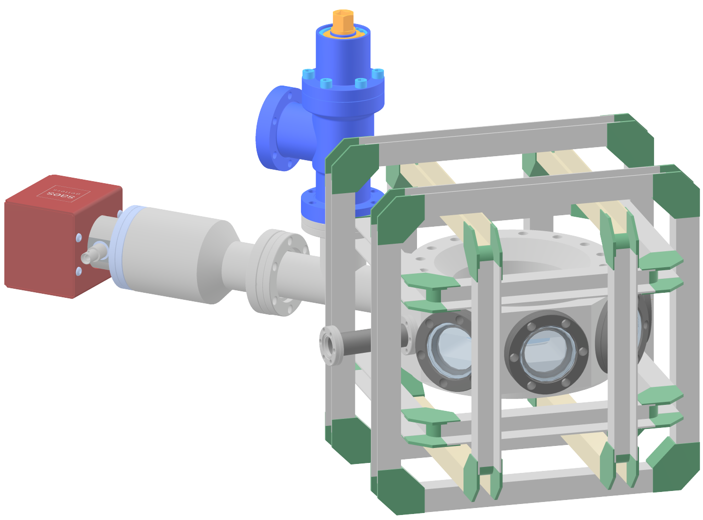

Figure 5.1: CAD model of the compensation coil system around the vacuum chamber. Here the importance of good optical access is evident as it can be seen by the amount and positioning of the viewports. The small flange on the left indicates the connection for a 2D MOT. The large tube at the back left of the picture shows the pump arm of the vacuum chamber, consisting of an angle valve for connecting a turbomolecular pump (blue) and a non-evaporable getter pump (red).

A Magnetic Field of Rectangular Coil Pair

The components of the magnetic field for a rectangular Helmholtz coils are obtained by using Equation 2.34, Equation 2.35 and Equation 2.35. Despite their length, they are explicitly stated here because they are a central, with regard to the uniform volume and the field strength, in designing the Helmholtz coil pairs.

$$
\begin{aligned}
B_x = \frac{\mu_0 I n}{4\pi} \Bigg[& \frac{(y+b)(z-d/2)}{\left((x-a)^2+(z-d/2)^2\right)\sqrt{(x-a)^2+(y+b)^2+(z-d/2)^2}} \\
& - \frac{(y+b)(z-d/2)}{\left((x+a)^2+(z-d/2)^2\right)\sqrt{(x+a)^2+(y-b)^2+(z-d/2)^2}} \\
& + \frac{(y-b)(z-d/2)}{\left((x+a)^2+(z-d/2)^2\right)\sqrt{(x+a)^2+(y-b)^2+(z-d/2)^2}} \\
& - \frac{(y-b)(z-d/2)}{\left((x-a)^2+(z-d/2)^2\right)\sqrt{(x-a)^2+(y-b)^2+(z-d/2)^2}} \\
& + \frac{(y+b)(z+d/2)}{\left((x-a)^2+(z+d/2)^2\right)\sqrt{(x-a)^2+(y+b)^2+(z+d/2)^2}} \\
& - \frac{(y+b)(z+d/2)}{\left((x+a)^2+(z+d/2)^2\right)\sqrt{(x+a)^2+(y-b)^2+(z+d/2)^2}} \\
& + \frac{(y-b)(z+d/2)}{\left((x+a)^2+(z+d/2)^2\right)\sqrt{(x+a)^2+(y-b)^2+(z+d/2)^2}} \\
& - \frac{(y-b)(z+d/2)}{\left((x-a)^2+(z+d/2)^2\right)\sqrt{(x-a)^2+(y-b)^2+(z+d/2)^2}} \Bigg]
\end{aligned}
\tag{A.1}
$$

$$
\begin{aligned}
B_y = \frac{\mu_0 I n}{4\pi} \Bigg[& \frac{(x+a)\,(z-d/2)}{\left((y-b)^2+(z-d/2)^2\right)\sqrt{(x+a)^2+(y-b)^2+(z-d/2)^2}} \\
& - \frac{(x+a)\,(z-d/2)}{\left((y+b)^2+(z-d/2)^2\right)\sqrt{(x+a)^2+(y+b)^2+(z-d/2)^2}} \\
& - \frac{(x-a)\,(z-d/2)}{\left((y-b)^2+(z-d/2)^2\right)\sqrt{(x-a)^2+(y+b)^2+(z-d/2)^2}} \\
& + \frac{(x-a)\,(z-d/2)}{\left((y-b)^2+(z-d/2)^2\right)\sqrt{(x-a)^2+(y-b)^2+(z-d/2)^2}} \\
& + \frac{(x+a)\,(z+d/2)}{\left((y-b)^2+(z+d/2)^2\right)\sqrt{(x+a)^2+(y-b)^2+(z+d/2)^2}} \\
& - \frac{(x+a)\,(z+d/2)}{\left((y+b)^2+(z+d/2)^2\right)\sqrt{(x+a)^2+(y+b)^2+(z+d/2)^2}} \\
& - \frac{(x-a)\,(z+d/2)}{\left((y-b)^2+(z+d/2)^2\right)\sqrt{(x-a)^2+(y+b)^2+(z+d/2)^2}} \\
& + \frac{(x-a)\,(z+d/2)}{\left((y-b)^2+(z+d/2)^2\right)\sqrt{(x-a)^2+(y-b)^2+(z+d/2)^2}} \Bigg]
\end{aligned}
\tag{A.2}
$$

$$
\begin{aligned}
B_z = \frac{\mu_0 I n}{4\pi} \Bigg[& \frac{(x+a)(y+b)}{\left[(y+b)^2 + (z-d/2)^2\right] \sqrt{(x+a)^2 + (y+b)^2 + (z-d/2)^2}} \\
& + \frac{(x+a)(y+b)}{\left[(x+a)^2 + (z-d/2)^2\right] \sqrt{(x+a)^2 + (y+b)^2 + (z-d/2)^2}} \\
& - \frac{(x+a)(y-b)}{\left[(y-b)^2 + (z-d/2)^2\right] \sqrt{(x+a)^2 + (y-b)^2 + (z-d/2)^2}} \\
& - \frac{(x+a)(y-b)}{\left[(x+a)^2 + (z-d/2)^2\right] \sqrt{(x+a)^2 + (y-b)^2 + (z-d/2)^2}} \\
& - \frac{(x-a)(y+b)}{\left[(x-a)^2 + (z-d/2)^2\right] \sqrt{(x-a)^2 + (y+b)^2 + (z-d/2)^2}} \\
& - \frac{(x-a)(y+b)}{\left[(y+b)^2 + (z-d/2)^2\right] \sqrt{(x-a)^2 + (y+b)^2 + (z-d/2)^2}} \\
& + \frac{(x-a)(y-b)}{\left[(x-a)^2 + (z-d/2)^2\right] \sqrt{(x-a)^2 + (y-b)^2 + (z-d/2)^2}} \\
& + \frac{(x-a)(y-b)}{\left[(y+b)^2 + (z-d/2)^2\right] \sqrt{(x-a)^2 + (y-b)^2 + (z-d/2)^2}} \\
& + \frac{(x+a)(y+b)}{\left[(y+b)^2 + (z+d/2)^2\right] \sqrt{(x+a)^2 + (y+b)^2 + (z+d/2)^2}} \\
& + \frac{(x+a)(y+b)}{\left[(x+a)^2 + (z+d/2)^2\right] \sqrt{(x+a)^2 + (y+b)^2 + (z+d/2)^2}} \\
& - \frac{(x+a)(y-b)}{\left[(y-b)^2 + (z+d/2)^2\right] \sqrt{(x+a)^2 + (y-b)^2 + (z+d/2)^2}} \\
& - \frac{(x+a)(y-b)}{\left[(x+a)^2 + (z+d/2)^2\right] \sqrt{(x+a)^2 + (y-b)^2 + (z+d/2)^2}} \\
& - \frac{(x-a)(y+b)}{\left[(x-a)^2 + (z+d/2)^2\right] \sqrt{(x-a)^2 + (y+b)^2 + (z+d/2)^2}} \\
& - \frac{(x-a)(y+b)}{\left[(y+b)^2 + (z+d/2)^2\right] \sqrt{(x-a)^2 + (y+b)^2 + (z+d/2)^2}} \\
& + \frac{(x-a)(y-b)}{\left[(x-a)^2 + (z+d/2)^2\right] \sqrt{(x-a)^2 + (y-b)^2 + (z+d/2)^2}} \\
& + \frac{(x-a)(y-b)}{\left[(y+b)^2 + (z+d/2)^2\right] \sqrt{(x-a)^2 + (y-b)^2 + (z+d/2)^2}} \Bigg]
\end{aligned}
\tag{A.3}
$$

B Blueprints

This appendix shows the technical sketches of the custom designed parts. The material used and all necessary measurements are included for future reference.

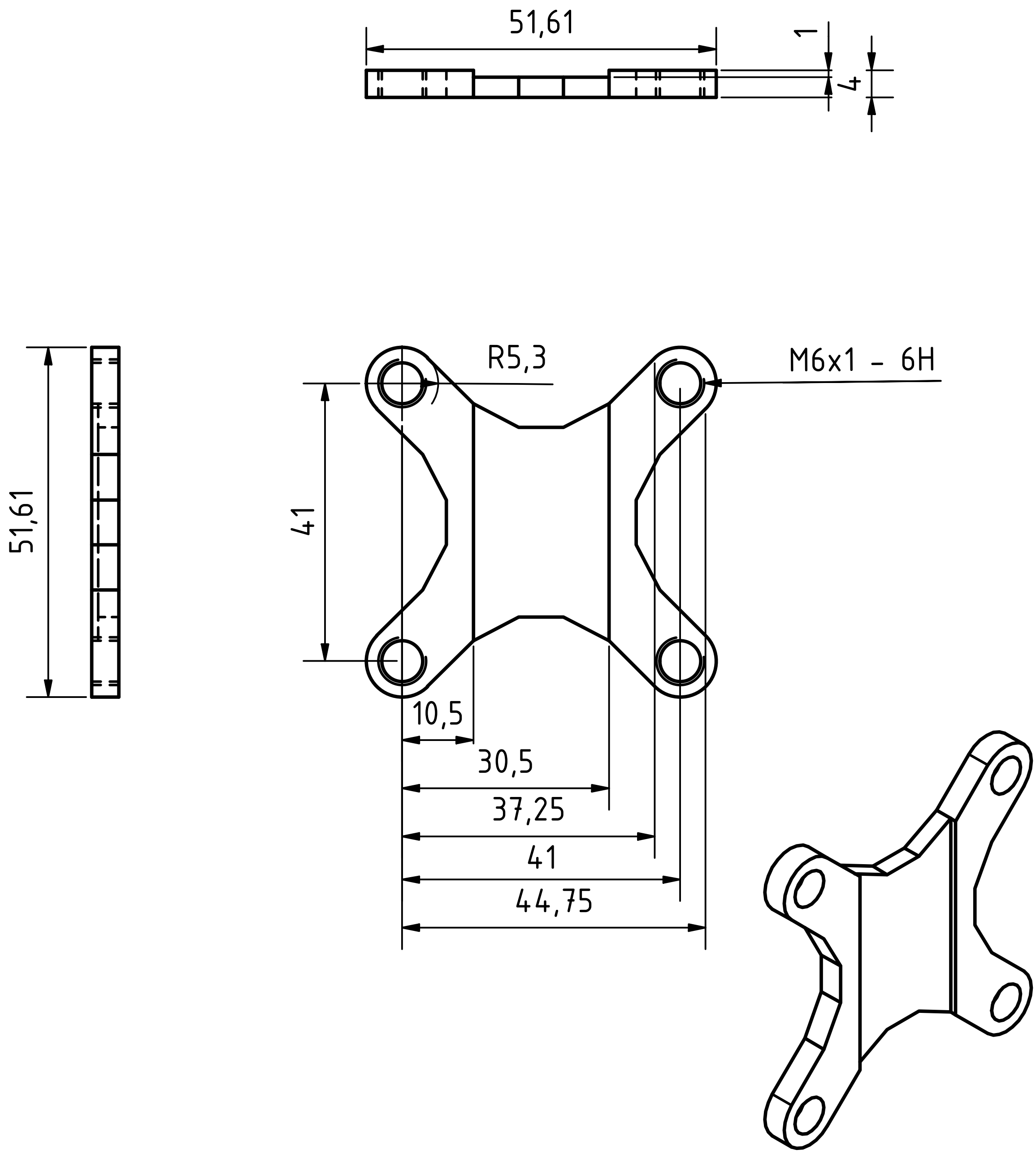

PI5		
Maßstab: 1 : 1	Einheiten: mm	
Material: Aluminuim		
X-Connector for adjacent Coils		1 von 1
Stückzahl: 1		A4

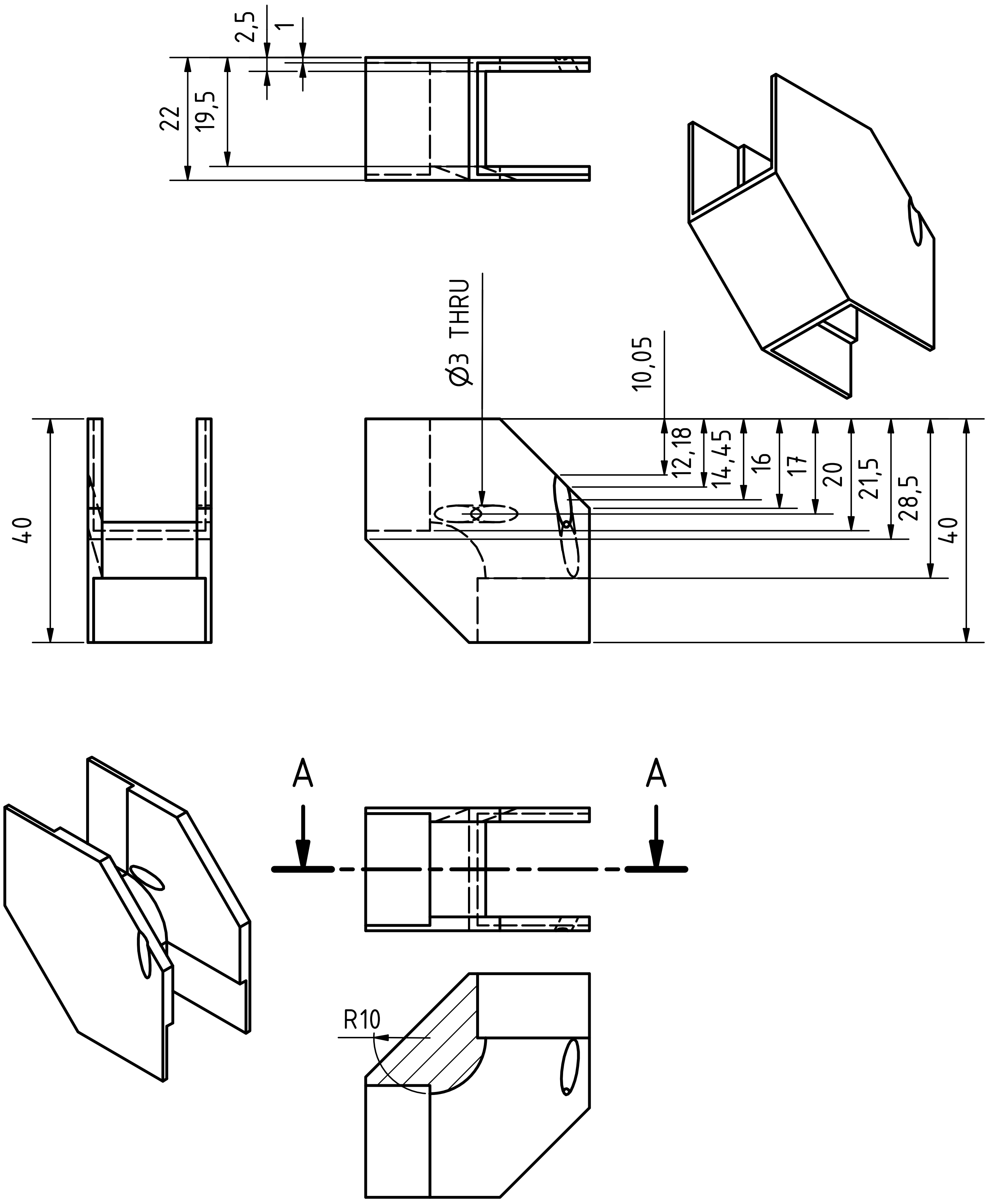

A-A (1 : 1)

PI5

Maßstab: 1 : 1

Einheiten: mm

Material: PLA (3D printed)

L-Connector with Inlet and Outlet

1 von 1

Stückzahl: 1

A4

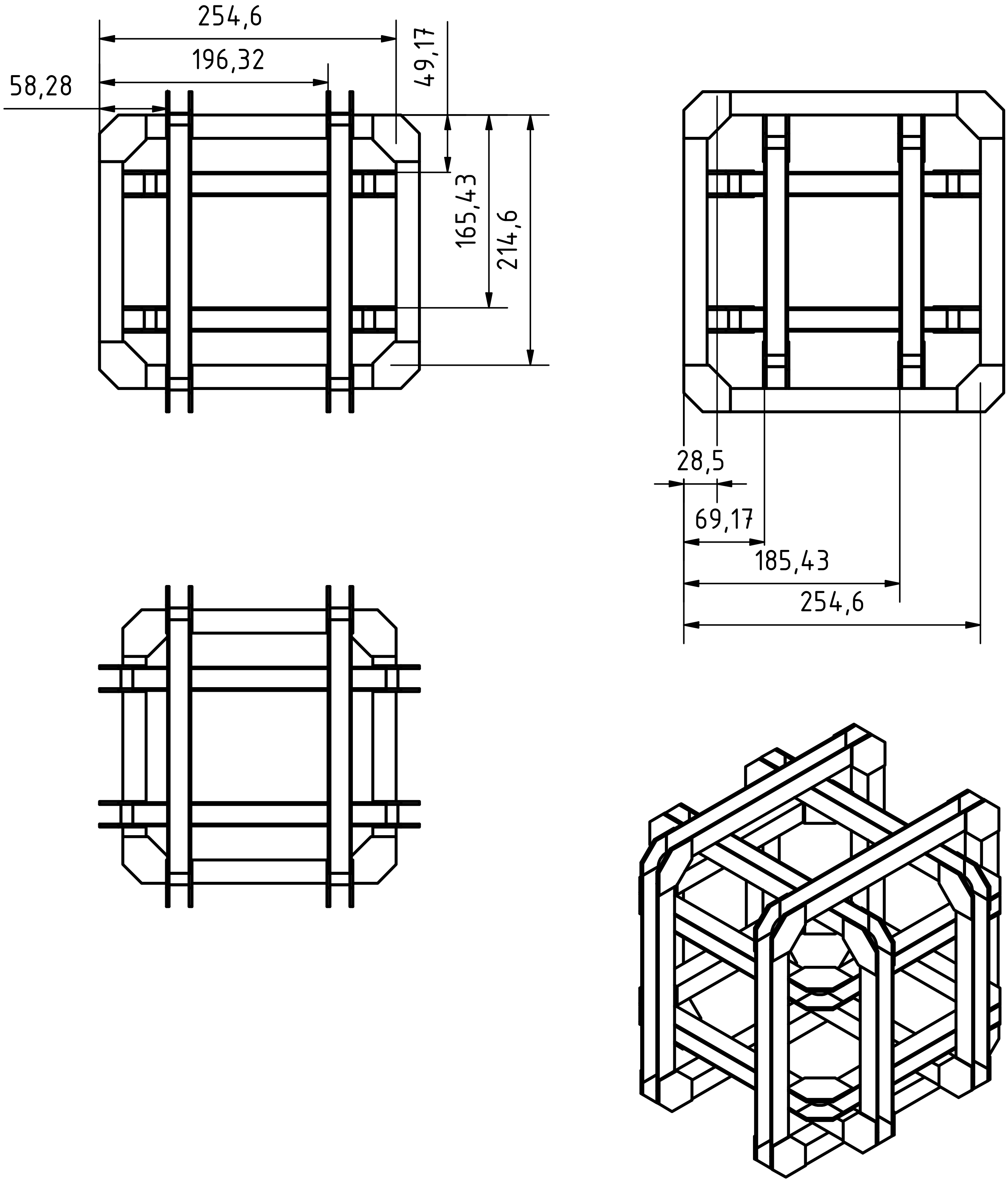

PI5

Maßstab: 1 : 5

Einheiten: mm

Material: Aluminium, PLA

Prototype Compensation Coil Cage

1 von 1

Stückzahl: 1

A4

Bibliography

[1] H Jeff Kimble. "The quantum internet". In: *Nature* 453.7198 (2008), pp. 1023–1030.

[2] Daniele Cuomo, Marcello Caleffi, and Angela Sara Cacciapuoti. "Towards a distributed quantum computing ecosystem". In: *IET Quantum Communication* 1.1 (2020), pp. 3–8.

[3] Valerio Scarani et al. "The security of practical quantum key distribution". In: *Reviews of modern physics* 81.3 (2009), pp. 1301–1350.

[4] Angela Sara Cacciapuoti et al. "Quantum internet: Networking challenges in distributed quantum computing". In: *IEEE Network* 34.1 (2019), pp. 137–143.

[5] Jens Eisert. "Entanglement in quantum information theory". In: *arXiv preprint quant-ph/0610253* (2006).

[6] Artur Ekert and Richard Jozsa. "Quantum algorithms: entanglement–enhanced information processing". In: *Philosophical Transactions of the Royal Society of London. Series A: Mathematical, Physical and Engineering Sciences* 356.1743 (1998), pp. 1769–1782.

[7] Philippe Allard Guérin et al. "Exponential communication complexity advantage from quantum superposition of the direction of communication". In: *Physical review letters* 117.10 (2016), p. 100502.

[8] Wojciech Hubert Zurek. "Decoherence, einselection, and the quantum origins of the classical". In: *Reviews of modern physics* 75.3 (2003), p. 715.

[9] L-M Duan and Christopher Monroe. "Colloquium: Quantum networks with trapped ions". In: *Reviews of Modern Physics* 82.2 (2010), pp. 1209–1224.

[10] Maximilian Ruf et al. "Quantum networks based on color centers in diamond". In: *Journal of Applied Physics* 130.7 (2021).

[11] Andreas Reiserer and Gerhard Rempe. "Cavity-based quantum networks with single atoms and optical photons". In: *Reviews of Modern Physics* 87.4 (2015), pp. 1379–1418.

[12] Stephan Welte et al. "Photon-mediated quantum gate between two neutral atoms in an optical cavity". In: *Physical Review X* 8.1 (2018), p. 011018.

[13] Bastian Hacker et al. "A photon–photon quantum gate based on a single atom in an optical resonator". In: *Nature* 536.7615 (2016), pp. 193–196.

[14] Severin Daiss et al. "A quantum-logic gate between distant quantum-network modules". In: *Science* 371.6529 (2021), pp. 614–617.

[15] Daniel Barredo et al. "An atom-by-atom assembler of defect-free arbitrary two-dimensional atomic arrays". In: *Science* 354.6315 (2016), pp. 1021–1023.

[16] L-M Duan and HJ Kimble. "Scalable photonic quantum computation through cavity-assisted interactions". In: *Physical review letters* 92.12 (2004), p. 127902.

[17] Philip Thomas et al. "Efficient generation of entangled multiphoton graph states from a single atom". In: *Nature* 608.7924 (2022), pp. 677–681.

[18] Daniel A Steck. "Rubidium 87 D line data". In: (2001).

[19] Ronald T Merrill, Michael William McElhinny, and Phillip L McFadden. *The magnetic field of the earth: paleomagnetism, the core, and the deep mantle*. Vol. 63. Academic Press, 1998.

[20] A. Herzenberg and Edward Crisp Bullard. "Geomagnetic dynamos". In: *Philosophical Transactions of the Royal Society of London. Series A, Mathematical and Physical Sciences* 250.986 (1958), pp. 543–583.

[21] Joseph Larmor and S Joseph. "Possible rotational origin of magnetic fields of Sun and Earth". In: *Elec. Rev* 85 (1919), p. 412.

[22] Christoph Clauser. *Einführung in die Geophysik*. Springer, 2014.

[23] Arnaud Chulliat et al. "The US/UK world magnetic model for 2020-2025: Technical report". In: (2020).

[24] Dipl.-Ing.(FH) Rainer Ketzler. *Messung des Erdmagnetfeldes in der PTB*. de. URL: https://www.ptb.de/cms/nc/ptb/fachabteilungen/abt2/fb-25/ag-251/live-daten-erdmagnetfeldmessung.html (visited on 04/01/2025).

[25] *Space Weather*. en. URL: https://www.swpc.noaa.gov/ (visited on 04/01/2025).

[26] John David Jackson. *Classical electrodynamics*. John Wiley & Sons, 1998.

[27] Wolfgang Demtröder. *Experimentalphysik*. Vol. 2. Springer, 2003.

[28] Xuehua Zhu et al. "Design of improved four-coil structure with high uniformity and effective coverage rate". In: *Heliyon* 9.4 (2023).

[29] Jorge Enrique García-Farieta and Alejandro Hurtado Márquez. "Exploring the magnetic field of Helmholtz and Maxwell coils: a computer-based approach exploiting the superposition principle". In: *Revista Brasileira de Ensino de Física* 42 (2020), p. 282.

[30] Werner Braunbek. "Die erzeugung weitgehend homogener magnetfelder durch kreisströme". In: *Zeitschrift für Physik* 88 (1934), pp. 399–402.

[31] Dejan M Petković and Milica D Radić. "Generalization of Helmholtz coil problem". In: *Serbian Journal of Electrical Engineering* 12.3 (2015), pp. 375–384.

[32] Carl Heller. "Über die Erzeugung großräumiger homogener Magnetfelder zum Studium des Verhaltens von Magnetkompassen und Kompensiermitteln auf verschiedenen magnetischen Breiten". In: *Deutsche Hydrographische Zeitschrift* 8.4 (1955), pp. 157–164.

[33] Andres F Restrepo Alvarez, Edinson Franco-Mejia, and Carlos R Pinedo-Jaramillo. "Study and analysis of magnetic field homogeneity of square and circular Helmholtz coil pairs: A Taylor series approximation". In: *2012 VI Andean Region International Conference*. IEEE. 2012, pp. 77–80.

[34] Torsten Fließbach. *Elektrodynamik: Lehrbuch zur Theoretischen Physik II*. Vol. 2. Springer-Verlag, 2012.

[35] Harley Flanders. "Differentiation under the integral sign". In: *The American Mathematical Monthly* 80.6 (1973), pp. 615–627.

[36] Richard Dengler. "Self inductance of a wire loop as a curve integral". In: *arXiv preprint arXiv:1204.1486* (2012).

[37] Frederick Warren Grover. *Formulas and tables for the calculation of the inductance of coils of polygonal form*. 468. US Department of Commerce, Bureau of Standards, 1923.

[38] Harold A Wheeler. "Inductance formulas for circular and square coils". In: *Proceedings of the IEEE* 70.12 (1982), pp. 1449–1450.

[39] Jake J Abbott. "Parametric design of tri-axial nested Helmholtz coils". In: *Review of scientific instruments* 86.5 (2015).

[40] Studiosus Kirchhoff. "Ueber den Durchgang eines elektrischen Stromes durch eine Ebene, insbesondere durch eine kreisförmige". In: *Annalen der Physik* 140.4 (1845), pp. 497–514.

[41] Colm T O'Sullivan. "Newton's law of cooling—A critical assessment". In: *Am. J. Phys* 58.10 (1990), pp. 956–960.

[42] Andrea del Carme Fontanet Valls. "Design and construction of a 3D Helmholtz coil system for the ALBA magnetic measurements laboratory". B.Sc. thesis. Universitat Politècnica de Catalunya, 2019.

[43] David R Lide. *CRC handbook of chemistry and physics*. Vol. 85. CRC press, 2004.

[44] Ranga Rosok. "Active Magnetic Field Stabisation for a Quantum Gas Microscope". B.Sc. thesis. University of Stuttgart, 2021.

[45] Jürgen Hagedorn, Florian Sell-Le Blanc, and Jürgen Fleischer. *Handbuch der Wickeltechnik für hocheffiziente Spulen und Motoren: ein Beitrag zur Energieeffizienz*. Springer-Verlag, 2016.

[46] Stefan Mayer. *Magnetic Field Sensor FLC3-70*. eng. Nov. 2021. URL: https://www.stefan-mayer.com/images/datasheets/Data-sheet_FLC3-70.pdf (visited on 03/28/2025).

[47] Avraham Shitzer. "Wind-chill-equivalent temperatures: regarding the impact due to the variability of the environmental convective heat transfer coefficient". In: *International journal of biometeorology* 50 (2006), pp. 224–232.

[48] Mahmoud Massoud. *Engineering thermofluids*. Vol. 2005. Springer, 2005.